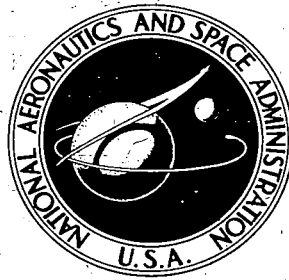


**NASA TECHNICAL
REPORT**



NASA TR R-193

21

LOAN COPY:

AFWL

KIRTLAND AFB

0068072



TECH LIBRARY KAFB, NM

**SHOCK-LAYER RADIATION
OF BLUNT BODIES
AT REENTRY VELOCITIES**

by William A. Page and James O. Arnold

Ames Research Center

Moffett Field, Calif.



0068072

SHOCK-LAYER RADIATION OF BLUNT BODIES
AT REENTRY VELOCITIES

By William A. Page and James O. Arnold

Ames Research Center
Moffett Field, Calif.

NATIONAL AERONAUTICS AND SPACE ADMINISTRATION

For sale by the Office of Technical Services, Department of Commerce,
Washington, D.C. 20230 -- Price \$1.25

TABLE OF CONTENTS

	<u>Page</u>
SUMMARY	1
INTRODUCTION	1
SYMBOLS	3
FACILITIES	5
Pilot Facility	6
Prototype Facility	6
Determination of Flight Parameters	7
Models	8
RADIOMETRIC INSTRUMENTATION	8
Description	8
Calibration	9
REVIEW OF THEORETICAL PREDICTIONS	10
Equilibrium Air Radiation	10
Nonequilibrium Air Radiation	12
NARROW-BAND RADIOMETER RESULTS	14
BROADBAND RADIOMETER RESULTS	17
Equilibrium Air Radiation	17
Nonequilibrium Air Radiation	20
COMPARISON OF NONEQUILIBRIUM RADIATION RESULTS WITH SHOCK-TUBE OBSERVATIONS	26
RADIATIVE HEATING OF FULL-SCALE VEHICLES	27
CONCLUDING REMARKS	30
APPENDIX A - THEORETICAL COMPUTATION OF TOTAL SPECTRAL RADIATION FROM SHOCK LAYER	32
APPENDIX B - DETERMINATION OF EFFECTIVE VOLUME FOR EQUILIBRIUM SHOCK LAYER	34
REFERENCES	37
TABLE	40

SHOCK-LAYER RADIATION OF BLUNT BODIES

AT REENTRY VELOCITIES

By William A. Page and James O. Arnold

Ames Research Center
Moffett Field, Calif.

SUMMARY

Measurements are presented of the thermal radiation from shock layers of models simulating vehicles entering the Earth's atmosphere. The data are analyzed and the contribution of radiative heating to the total heating loads imposed upon entry vehicles is evaluated.

The models were launched by light-gas guns into still air or into a countercurrent air stream generated by a shock-tube-driven hypersonic wind tunnel. Velocities ranged from 5.4 to 12.4 km/sec, some 1.5 km/sec above the velocity for Earth escape while free-stream densities were varied over a range of 1000 to 1, from $\rho_{\infty}/\rho_0 = 2 \times 10^{-4}$ to 2×10^{-1} . Various types of radiometric measurements led to estimates of the total radiation and the spectral distribution of the radiation.

Results from the present experiments for air in thermodynamic and chemical equilibrium correspond typically to within a factor of 2 to the theoretical and experimental work in the literature. Measurements of the thermal radiation emitted from the nonequilibrium reaction zone directly behind the bow shock give characteristic radiative heating fluxes of 2, 6, and 18 watts/cm² for velocities of 6.4, 9.5, and 11.0 km/sec, respectively. These nonequilibrium heating intensities are considerably below early estimates of nonequilibrium heating. The values are not expected to change with flight density or vehicle size.

The report also includes a discussion based on laboratory results of methods for predicting radiative heating of full-scale vehicles. Included are remarks regarding special problems, such as collision limiting, merging of shock layer and boundary layer, radiation self-absorption, and flow energy limiting, which must be considered when the present results are extended far from the test conditions.

INTRODUCTION

For several years now, it has become increasingly apparent that, as the speed of vehicles entering the Earth's atmosphere approaches or exceeds the Earth escape value, radiative heating from the shock layer, namely the heated air between the bow shock and the body surface, can contribute significantly to

the total vehicle heating. In fact, estimates of radiative intensities have indicated that this form of heating, rather than convective heating, will, in certain cases, become predominant at entry velocities above Earth escape speed. Interest in entry at greater than Earth escape speed comes from studies of the return of vehicles from the nearby planets, such as Mars or Venus.

An extensive effort, of which the present study is a part, has been in progress to determine the parameters controlling radiative heat transfer to entry vehicles from the shock layer about the body. Various problem areas require study. With knowledge of the thermodynamic and chemical properties of the gas in the shock layer and fundamental data on the radiation from the gas as a function of these properties, it is possible to determine the radiation falling on the body surface. Only a portion of the radiation is absorbed, depending upon the absorptivity of the surface material to the incident radiation. There are, of course, other complicating features, such as radiation self-absorption, flow energy limiting, lack of thermodynamic and chemical equilibrium in the shock layer, coupling of the convective, radiative, and ablative processes, etc., all of which require investigation before accurate predictions of full-scale radiative heating loads can be made.

Early contributions to the problem of predicting thermal radiation from the constituents of high temperature air are exemplified by the theoretical work of Meyerott in 1955 (ref. 1) and of Kivel, Mayer, and Bethe in 1957 (ref. 2). The study entered an important phase with the publication of several estimates of the total thermal radiation from air in thermodynamic and chemical equilibrium (Kivel and Bailey, 1957, ref. 3, and Meyerott, et al., 1959, ref. 4). These papers emphasize, for the most part, molecular band radiators at intermediate gas temperatures (typically 1,000° to 12,000° K). Radiation from equilibrium air at higher temperatures has been studied theoretically by Armstrong, 1958 (ref. 5).

Of the basic laboratory methods utilized to investigate the thermal radiation from high temperature gases, use of the shock tube has contributed an important portion of the information required to assign absolute radiative intensities to the various species contributing to the total radiation from air (see, e.g., refs. 3 and 4). A particular advantage of shock-tube tests is the nominal one-dimensional flow which permits spatial resolution of the radiation in the reaction zone directly behind the shock wave. Such experiments have added significantly to our knowledge of the radiative properties of the nonequilibrium air behind the shock which has not yet reached conditions of thermodynamic and chemical equilibrium.

The studies reported here were begun in 1959 and had as an objective to obtain experimental data on the radiative intensities from air in the shock layer of bodies in flight at very high speeds. Of particular interest was the effect of speed on the radiation in the range from earth satellite speed up to and beyond earth escape speed. The effect of ambient density was also of interest, as well as the level of intensity of the nonequilibrium component of the radiation. Similar work was then going on in the shock-tube facilities mentioned above, and it was desired both to extend the range of velocity and density beyond those attained in the shock tubes where possible and also to provide

a set of measurements by an independent technique. The present data cover a velocity range from 5.5 to 12.4 km/sec and a free-stream density range from $\rho_\infty/\rho_0 = 2 \times 10^{-4}$ to 2×10^{-1} . The free-stream density range was sufficient so that the air in the shock layer was (a) in essentially complete thermodynamic and chemical equilibrium at high densities and (b) in a highly nonequilibrium state at low densities. These conditions allowed study of the radiation from both equilibrium and nonequilibrium gas samples. Some of the earlier results from this study were previously reported in references 6 and 7. A summary of the present results was given in reference 8.

SYMBOLS

A_{eff}	effective radiating area, cm^2 , defined by equation (12)
A_{total}	spherical face area of model, cm^2
C_p	pressure coefficient
d	model diameter, cm
e	voltage output of radiometer, volts
E	radiative intensity per unit volume, watts/cm^3
E_{eq}	radiative intensity from equilibrium gas, watts/cm^3
E_p	peak radiative intensity in nonequilibrium zone, watts/cm^3
E_t	radiative intensity behind normal shock, watts/cm^3
E_λ	spectral radiative intensity, watts/cm^3 micron
F	fraction of total radiation responded to by broadband radiometer
I	radiative intensity integrated along stagnation streamline, watts/cm^2 , defined by equation (10)
k	shock-layer shape correction factor
K	radiometer calibration constant, volts/watt
L_λ	spectral radiation from standard lamp, watts/micron
p_0	sea-level atmospheric pressure
p_s	wind-tunnel reservoir pressure
p_{t2}	pitot pressure
\dot{q}_R	stagnation-region radiative heating rate, watts/cm^2

r, θ	polar coordinate system in plane passing through model axis of symmetry (see fig. 13)
r_2	shock-wave radius, cm
R	body nose radius, cm; gas constant, cal/gm $^{\circ}$ K
R_{λ}	relative spectral response of radiometer ($R_{\lambda_{\max}} = 1$)
t_E	excitation time of nonequilibrium radiation pattern to E_p , sec
t_R	relaxation time of nonequilibrium radiation pattern to 1.1 E_{eq} , sec
T	equilibrium temperature behind normal shock wave, $^{\circ}$ K
T_0	atmospheric sea-level reference temperature, 288 $^{\circ}$ K
T_{λ}	spectral transmission of optical filter
U_{∞}	wind-tunnel stream velocity, km/sec
V_{eff}	effective radiating volume, cm 3 , defined by equation (8)
V_{total}	total shock-layer volume, cm 3 , defined by equation (B6)
V_{∞}	total velocity, km/sec
W_t	total radiant flux from volume of shock layer in view of radiometer, watts
W_{obs}	portion of W_t spectrally observed by broadband radiometer, watts
W_{λ}	spectral radiant flux from shock layer, watts/micron
δ	shock-wave standoff distance, cm
δ_E	excitation distance of nonequilibrium radiation pattern to E_p , cm
δ_R	relaxation distance of nonequilibrium radiation pattern to 1.1 E_{eq} , cm
λ	wavelength, microns
ρ	equilibrium air density behind normal shock wave
ρ_{∞}	free-stream air density
ρ_0	sea-level atmospheric density

FACILITIES

The technique developed to obtain the high velocities required for this investigation consisted of launching small plastic or metal models from light-gas guns into either still air or into the air stream developed by a shock-tube-driven hypersonic nozzle. Two facilities were used, the pilot hypersonic free-flight facility, and the prototype hypersonic free-flight facility, both of Ames Research Center. The pilot and prototype facilities, which are similar except for size and complexity, are shown schematically in figures 1 and 2, respectively.

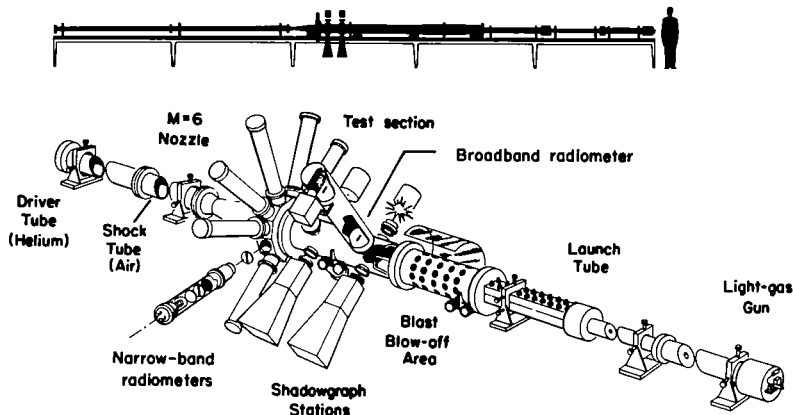


Figure 1.

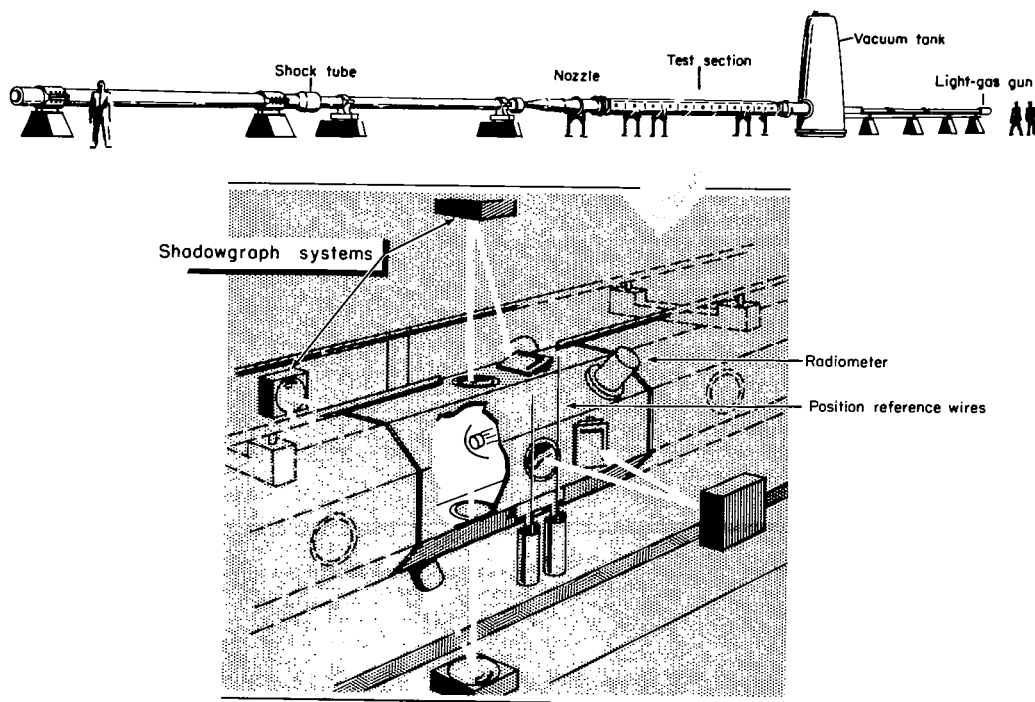


Figure 2.

Pilot Facility

The pilot facility employs a two-stage shock-heated 7.1-mm bore light-gas gun, which is capable of launching models to muzzle velocities of 8.8 km/sec.

The 1.8 km/sec countercurrent air stream is generated by a hypersonic nozzle contoured to produce uniform flow at a Mach number of 6. The reservoir air required is heated in a cold-helium-driven shock tube of 7 meter total length and 10 cm diameter. The shock tube is operated under tailored interface conditions and provides operating times of 2 to 3 milliseconds of uncontaminated air in the test section. Stream densities in the pilot facility ranged from $\rho_{\infty}/\rho_0 = 2 \times 10^{-3}$ to 6×10^{-2} with operation of the countercurrent air stream and from 2×10^{-4} to 2×10^{-1} under still air conditions. The facility and its operation are further described in reference 6.

Prototype Facility

The prototype facility is a larger version of the pilot facility and is designed to give aerodynamic and radiation data at Earth escape speed and higher. The facility utilizes an isentropic compression-heated light-gas gun of 12.7 mm bore similar to the gun described in reference 9. Launch velocities of 9.2 km/sec have been obtained.

The countercurrent stream is generated by a hypersonic nozzle contoured for Mach number 7. The reservoir stagnation conditions are obtained with a tailored interface shock tube driven with a combustible mixture of hydrogen, oxygen, and helium. The hydrogen and oxygen react giving a driving gas for the shock tube consisting principally of hot helium. Free-stream velocities of 1.8, 2.7, and 3.6 km/sec are available, depending upon adjustment of the nozzle area ratio, the operating pressure ratios in the shock tube, and the temperature of the driving gas. Data for this report from the prototype facility were obtained with the 3.6 km/sec air stream. The combined velocity obtained in the facility has reached 12.4 km/sec.

The driver and driven tubes have the same nominal dimensions, an internal diameter of 15.7 cm and a length of 12.2 meters. During the present investigation stagnation pressures varied from 8 to 260 atmospheres at a nominal stagnation enthalpy h/RT_0 of 90. These conditions resulted in free-stream densities, ρ_{∞}/ρ_0 , ranging from 2×10^{-4} to 10^{-2} in the 61-cm diameter by 12.2 meter long test section. A large dump tank incorporating a poppet valve depicted in figure 2 serves the same purpose as the blast blow-out patch in the pilot facility; namely, to relieve pressures inside the test section of the facilities at the termination of operation. A report of some of the development tests performed in the combustion chamber for the prototype facility is given in reference 10. Further description of the facility and its operating cycle can be found in reference 11.

Determination of Flight Parameters

Model velocity, position, and attitude for both facilities were obtained by conventional ballistic range instrumentation, namely, shadowgraph stations and electronic-counter timing equipment. When the facilities were operated with the countercurrent air stream, stream properties were determined by the following procedures. Total enthalpy and other stagnation region state variables of the air used to drive the wind tunnel are determined from measurements of the heating process in the shock tube. The state variables are defined by measurements of the initial charging pressures and temperatures, velocity of the incident shock, and the transient history of stagnation-region pressures in the shock tube. The stagnation air expands down the hypersonic nozzle to the test section where the transient history of static pressure at the wall is measured. With an assumed isentropic expansion process, all other free-stream properties, in particular velocity and density, can be computed. Redundant measurements were made of the center-line pitot pressure and the free-stream Mach number, the latter determined from shadowgraphs of the flow field about a fixed cone model mounted on the center line of the test section. These measurements show that the flow properties have been reasonably well determined. As an example, the table below gives results obtained in the prototype facility during several calibration runs at 3.6 km/sec of the pitot pressure as determined from measurement and as determined from computations based upon measurement of stagnation conditions and free-stream static pressure.

$\frac{P_{t2}}{P_o} = \frac{C_p}{2P_o} \rho_\infty U_\infty^2$		
Run	Measured	Computed with $C_p = 1.90$
151	1.33	1.50
152	1.29	1.12
153	1.16	1.24
154	1.16	1.29

It should be remarked that at the lower values of operating stagnation pressures, no evidence was found of lack of thermodynamic equilibrium in the flow discharged from the wind-tunnel nozzle. Further, radiative data obtained in the prototype facility at $V_\infty \sim 9.5$ km/sec and at $\rho_\infty/\rho_o \sim 4 \times 10^{-4}$ (see table I), with and without the air stream in operation, gave closely comparable results.

The instrumentation used for the transient pressure measurements discussed above were quartz-crystal rapid-response pressure transducers in the stagnation region of the shock tube and flush-diaphragm resistance strain-gage pressure transducers in the test section. Output traces from the transducers were displayed on cathode-ray oscilloscopes and were photographed. A typical set of

pressure records from the prototype facility is shown in figure 3. A typical set of records from the pilot facility were previously shown in reference 6.

Models

The models launched by the light-gas guns consisted of spherically nosed bodies as diagrammed in figure 4. Models made of plastic were machined in the cylindrical form while the aluminum models were subcaliber and launched in plastic sabots.

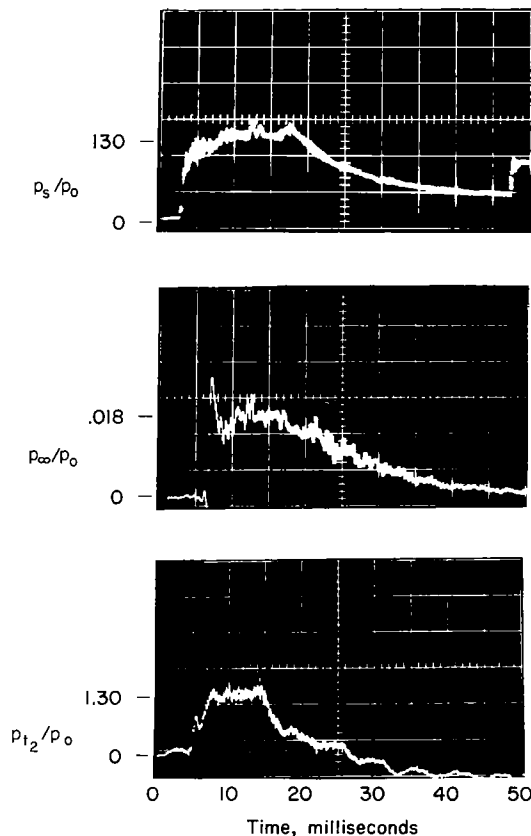


Figure 3.

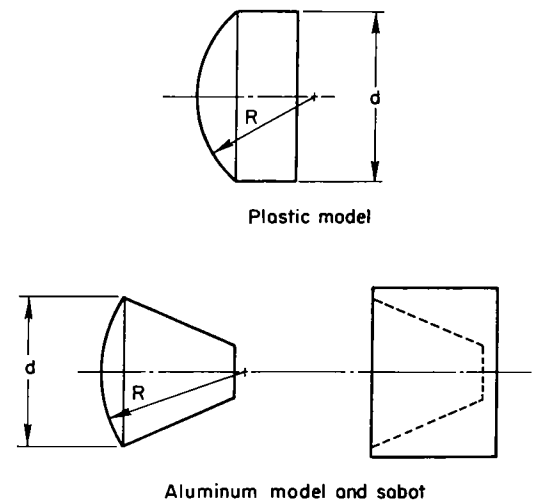


Figure 4.

RADIOMETRIC INSTRUMENTATION

Description

The radiation emitted from the model shock layer was measured with a variety of radiometers consisting of both broadband photomultiplier detectors and a series of eight narrow-band radiometers consisting of photomultiplier,

narrow-band optical filter combinations. The relative spectral response of the radiometers is depicted in figure 5, which also shows a typical spectrum from air in thermodynamic and chemical equilibrium from reference 4.

The instruments viewed the model at right angles to the flight path through narrow slit assemblies as is shown approximately to scale in figure 6. Slit widths of 7 mm in the pilot facility and 13 mm in the prototype facility were chosen to allow sufficient spatial resolution to differentiate the shock-layer radiation from that of the wake. Included in figure 6 is a typical phototube output oscilloscope trace, along with a self-luminous photograph (exposure time, 0.05 microsecond) of a model in flight. The narrow-band radiometers and one broadband radiometer were mounted on the pilot facility as shown in figure 1. Six broadband radiometers were located along the prototype facility test section as depicted in figure 2.

Calibration

Intensity of the radiation observed during the experiments was established by calibration of the radiometers with a radiant source of known absolute spectral intensity. The source was a tungsten ribbon filament lamp calibrated by the National Bureau of Standards (cf. ref. 12). Response of a radiometer to the standard lamp is given by

$$e = K \int_0^{\infty} R_{\lambda} L_{\lambda} d\lambda \quad (1)$$

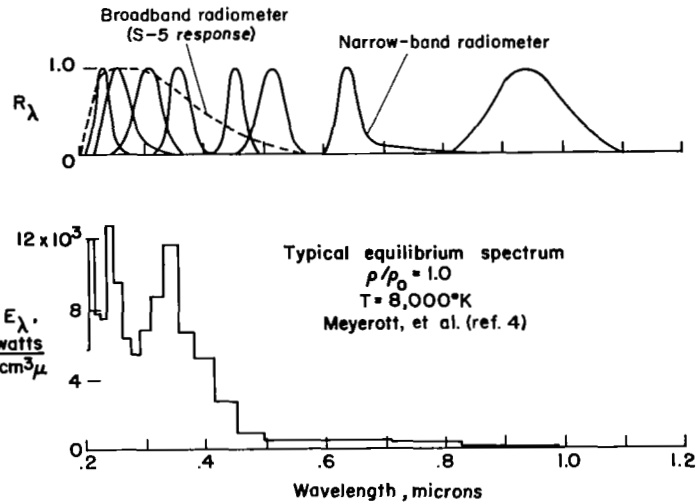


Figure 5.

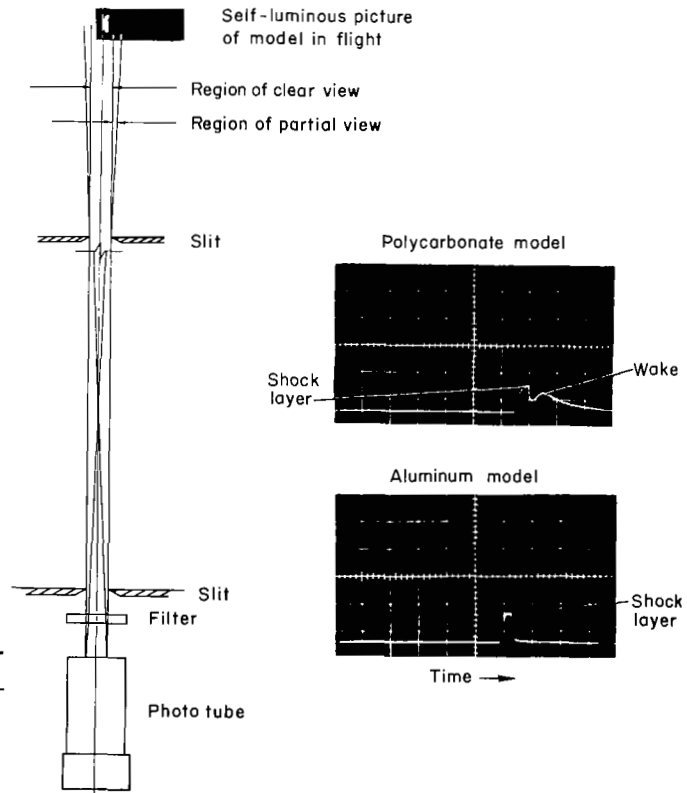


Figure 6.

where e is measured radiometer output in volts, K is the calibration constant in volts/watt, R_λ is the relative spectral response of the radiometer ($R_{\lambda_{\max}} = 1$), and L_λ is the spectral output of the standard lamp in watts/micron. The value of K is inversely proportional to the square of the distance from the source to the photocathode of the radiometer. To check this proportionality the radiometers were calibrated at various distances, including, for some radiometers, the distances actually used during testing. For the broadband radiometers, R_λ is the response of the phototube alone and was obtained from manufacturer's literature. For the relatively narrow-band radiometers, R_λ is given by

$$R_\lambda = \frac{R_\lambda' T_\lambda}{(R_\lambda' T_\lambda)_{\max}} \quad (2)$$

where T_λ is the absolute spectral transmission of the narrow-band optical filter, and R_λ' is, in this expression, the phototube response. Optical transmission of the filters was obtained by comparing response of a phototube irradiated with a monochromatic light beam with and without the filter present. At short wavelengths, scattering of light within the monochromators is troublesome, and, on occasion, several monochromators in series were used to obtain a pure monochromatic beam.

When the radiometers observe the model shock layer, the response is

$$e = K \int_0^\infty R_\lambda W_\lambda d\lambda \quad (3)$$

where W_λ , watts/micron, is the spectral radiant flux from that portion of the model shock layer in view of the radiometer. For the narrow-band radiometers, approximations to the values of W_λ were obtained by letting

$$\int_0^\infty R_\lambda W_\lambda d\lambda = W_\lambda \int_0^\infty R_\lambda d\lambda \quad (4)$$

Thus, W_λ was assumed to have a single value over the bandpass of the filter.

REVIEW OF THEORETICAL PREDICTIONS

Equilibrium Air Radiation

For completeness, we have included here a very brief and simplified review of the work that has been done to develop predictions for the intensity of thermal radiation from air in thermochemical equilibrium. Predictions have been made by a number of investigators, which, while differing in some of the details, have produced results in reasonable agreement, usually within a factor of 2. We will not presently investigate in any detail the reasons for the

remaining differences, but will confine our remarks to (a) a brief description of how the radiation predictions are generated, and (b) a graph of existing results as a function of temperature and density of the radiating gas.

The process of developing theoretical predictions consists of calculating the radiation intensity from a unit amount of each species present, and then, with knowledge of the equilibrium composition of the air, adding up the various contributions to obtain the total radiation. The determination of the radiative intensity as a function of temperature from a particular species is mathematically difficult and has led to various simplifications and, in most cases, to the necessity of determining experimentally an unknown parameter in the equations for the intensity. For example, the radiative intensity from a single excited electronic state of a molecule can be expressed as (see, e.g., ref. 13)

$$E \sim P n h \nu \quad (5)$$

where E is the radiative intensity, P is the transition probability (Einstein A coefficient) of an electronic transition, n is the number of molecules in the excited electronic state, h is Planck's constant, and ν is the frequency of the resultant radiation. The transition probability, in turn, may be approximated by

$$P \sim (h\nu)^2 f_e f_v f_r \quad (6)$$

where P has now been factored into three components related to the electronic, vibrational, and rotational excitation of the molecule. All but one of the components of the probability function can be computed from reasonable models of the molecular structure by use of wave mechanics. Usable values of the remaining transition probability, the electronic f number, have thus far only been determined from experiment. A multiplicity of such expressions must be summed, usually with simplification as to the wavelength structure of the radiation, to obtain an estimate of the total radiation from a given molecular species. Radiation caused by the interaction of free electrons with neutral or ionized particles (so-called free-free or free-bound sources) is normally approximated with the well-known classical Kramer's formula (cf. ref. 14). The adjustable parameter here is the effective charge Z of the particle involved in the interaction. Again, Z can be adjusted to fit experiment to theory. The available predictions for equilibrium air radiation are therefore, in a sense, hybrid in that they consist of a mixture of theory and experiment.

It should be remarked that the species causing the predominant radiation varies with temperature. For example, at temperatures of $5,000^\circ$ to $7,000^\circ$ K, the NO-beta and NO-gamma molecular bands have large contributions; at temperatures of $7,000^\circ$ to $9,000^\circ$ K, the N_2^+ -first negative molecular band is important; whereas increasing ionization at temperatures above $10,000^\circ$ K causes free-free and free-bound radiation from the neutral and ionized atoms of N and O to have a large contribution to the total radiation.

Figure 7 presents three available predictions for equilibrium radiation as a function of the temperature and density of the radiating gas taken from references 3, 4, and 15. The figure was produced by (a) reading directly figures 1 and 2 of reference 3 and noting that the quantity plotted is one-half the total radiation, E_t , (b) multiplying the absorption coefficients of reference 4 by Planck's black-body function and integrating the results to obtain the total radiation, and (c) reading directly figure 3 of reference 15 and noting that the quantity plotted must be multiplied by 4π to obtain the total radiation, E_t , in watts/cm³. These predictions are understood to be for radiation from an optically thin gas sample; no self-absorption of the radiation is considered.

Inspection of the figure shows that the three predictions are in fair agreement. In general, greater differences exist at the highest temperatures for all densities and at the lowest densities for all temperatures shown. It should be remarked, however, that the early results given in reference 3 are now considered by the authors thereof to be somewhat too high (ref. 16) at the highest temperatures shown.

The variation of E_t with temperature and density indicates that in the central region of the figure the radiation varies as $\rho^{1.3}$ and T^{12} . At the highest temperatures shown, the temperature dependence has dropped to T^8 . It should be remarked that the density dependence quoted above is obtained for constant temperature of the radiating gas. A different exponent is appropriate, as will be shown later when the velocity of the shock-wave heating the gas is held constant.

Nonequilibrium Air Radiation

Nonequilibrium radiation greater than the equilibrium intensity levels has become a well-recognized feature of photometric observations of high-speed shock-wave structure, both in shock tubes (cf. ref. 17) and in ballistic ranges (cf. ref. 6). A satisfactory theory capable of predicting the magnitude of this nonequilibrium radiation has not yet been developed. On the other hand, certain features of the radiation have been measured and a descriptive model of the radiative properties of the nonequilibrium zone behind a normal shock has been proposed by workers at Avco-Everett Laboratories (refs. 17, 18, and 19). Further, extensive computations (machine-programmed) leading to estimates of the thermodynamic and chemical properties of the nonequilibrium zone, behind both normal shocks and vehicle bow shocks, have been developed at Cornell Aeronautical Laboratories (cf. ref. 20).

Figure 8 is a schematic representation of the nonequilibrium zone model behind a normal shock wave, showing the variations of temperature, density, and radiative intensity as functions of distance behind the shock front. Directly behind the shock front very high translational temperatures exist, approaching the values in a perfect gas. The density jump across the shock front is initially close to the perfect gas value. Further downstream,

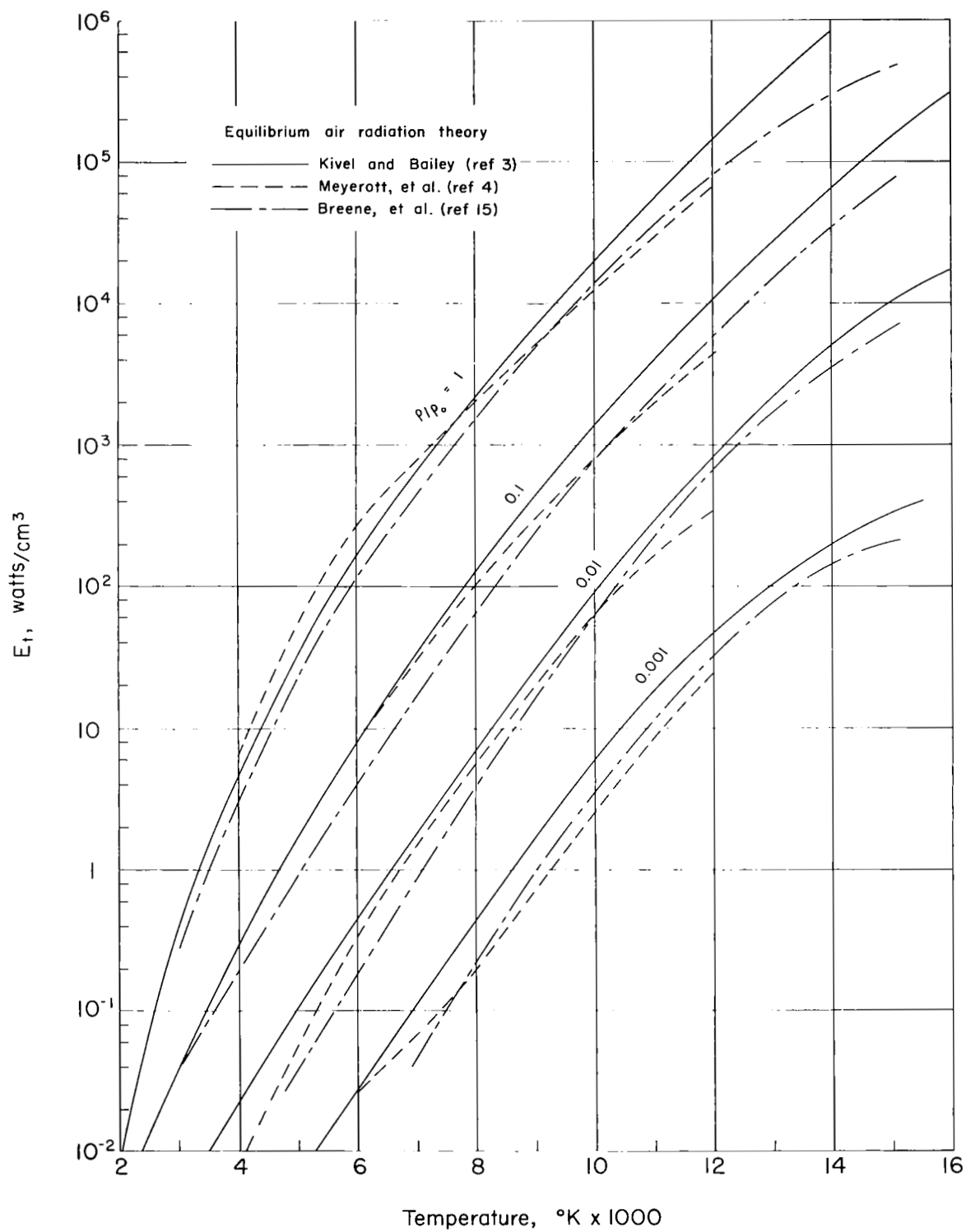


Figure 7.

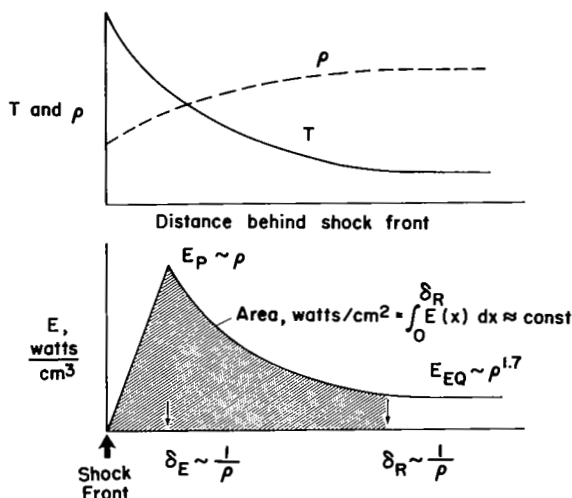


Figure 8.

equilibrium level. It is argued in reference 17 that the majority of the collisions exciting electronic states are binary (two-body collisions). The number of collisions per unit volume thus varies as the square of the particle density. However, the thickness of the reaction zone varies inversely with the density, leading to the relations depicted on the figure; namely, (a) the peak radiation, E_p , varies with density, and (b) the excitation distance, δ_E , and the relaxation distance, δ_R , vary inversely with the density. These relations then lead to the result that the total radiative output in watts/cm² (i.e., an integration of the radiation over the reaction zone, δ_R) per unit frontal area of the normal shock will be independent of density. This result applies approximately when the peak radiation, E_p , is large compared with the equilibrium level, and as long as binary collision processes are predominant. Evidence supporting this descriptive model can be found in references 18 and 19. It is also clear from the figure that the nonequilibrium radiation overshoot becomes more pronounced when free-stream density is decreased, because the level of equilibrium radiation varies approximately with $\rho^{1.7}$, at constant velocity (ref. 6), whereas the overshoot magnitude varies with ρ .

electronic excitation, vibration, dissociation, ionization, and formation of new species take place until the thermochemical equilibrium conditions of the gas are finally reached. During these overlapping processes, loss of energy from the translational mode reduces the translational temperature and the temperature and density approach the equilibrium values. The high temperatures existing near the shock front cause a strong radiation overshoot, as depicted in the figure. There is an excitation time for the radiation to build up to its peak value, believed to be closely related with the time required to populate excited electronic states, and then a relaxation (or decay) time for the radiation to decay to the

NARROW-BAND RADIOMETER RESULTS

The oscilloscope records from the radiometers (see, e.g., fig. 6) may be interpreted as follows: The first pulse represents radiation from the model shock layer. The second pulse is the wake. The approximate level portion of the first pulse is the stay time of the shock layer in the field of complete view, and the slow rise of the signal during this period is associated with radiation along the model sides coming into view. This interpretation is consistent with timing information obtained from shadowgraphs of the model flight and the rate of sweep of the oscilloscope records. Further, traces from observation of plastic models display the slow rise; aluminum models do not. This rise has been interpreted as the effect of ablation vapors flowing along the

cylinder model edge (ref. 21). Measurements of the radiation from the model shock layer were made from the traces at the beginning of the slow rise.

Presented in figure 9 and selected from the many which were obtained are low resolution spectra provided by the narrow-band radiometers. The observed radiation, W_λ , is plotted as a function of wavelength λ for several velocities, free-stream densities, and model materials. A line has been drawn through the symbols to represent the spectrum. Since it was not always possible to experimentally repeat velocities exactly, slight adjustments in W_λ have been made to correct the data on any given figure to the same reference velocity. The correction, never exceeding 9 percent, was deduced from the general trend of the data with velocity. The materials of which the models were machined were aluminum, polyethylene (trade name, Fortiflex), General Electric 124 and 123b (epoxy materials intended to perform as charring ablators), and a polycarbonate (trade name, Lexan). The spectra were selected to show the effect of density at a velocity near 6 km/sec where many spectra were available. The additional spectrum at 10.2 km/sec was included to show velocity effect.

Included on the figures are theoretical predictions for the observed radiation, W_λ , obtained from the equilibrium air radiation calculations of Meyerott, et al. (ref. 4) and Kivel and Bailey (ref. 3). Basically, the equilibrium prediction for W_λ is obtained by calculating the equilibrium thermodynamic values of temperature and density in the bow-shock-layer region, assigning

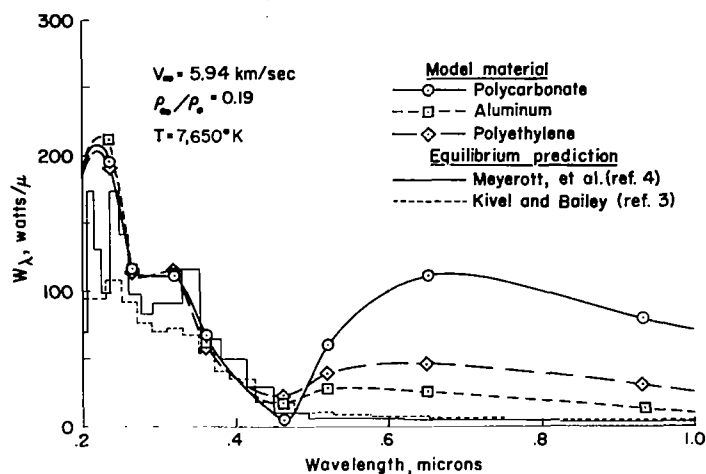


Figure 9(a).

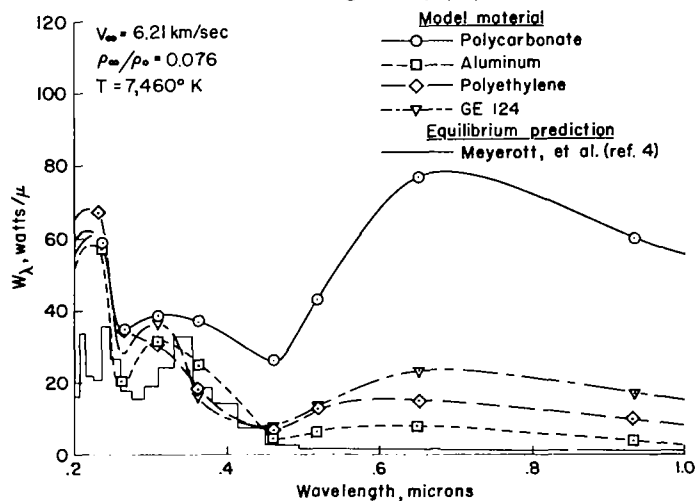


Figure 9(b).

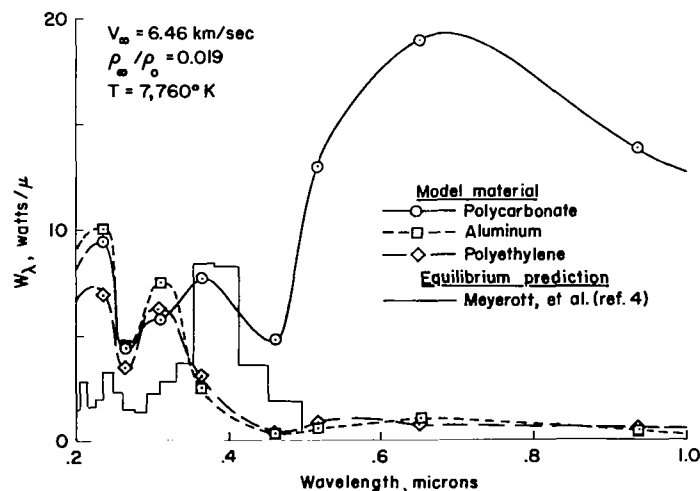


Figure 9(c).

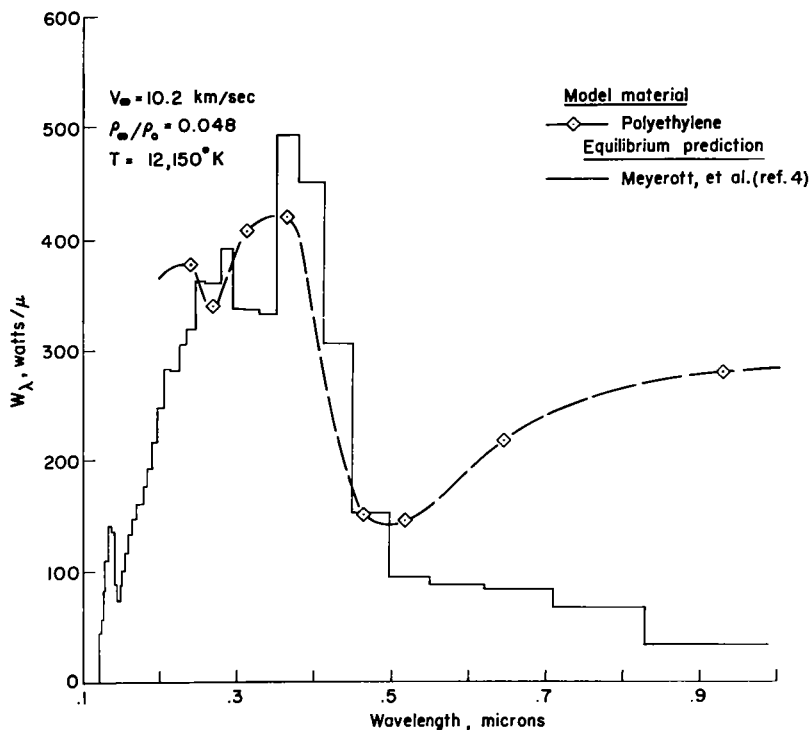


Figure 9(d).

values of radiative intensity to each volume element, and then integrating over the volume in view of the radiometer. Details of this process, including the approximations made, are described in appendix A.

Figure 9 brings to attention certain systematic effects which are remarked upon below: (a) the experimental spectra in the ultraviolet, 0.2 to 0.5 micron, is closely comparable for all model materials for a given set of flight conditions. An exception is polycarbonate at low flight densities. (b) In contrast, the radiative intensity in the infrared, 0.5 to 1.0 micron, depends

significantly upon model material. Polycarbonate exhibits the higher values of radiation, whereas aluminum exhibits the lower values. (c) The theoretical predictions of W_λ compare favorably, both from the standpoint of spectral shape and intensity, with the experimental spectra in the ultraviolet at the higher flight density, figure 9(a). The comparison degenerates at 6 km/sec as the density is lowered. The reason for the low estimate at low flight densities given by the equilibrium theory has been previously recognized (ref. 6) as due to the appearance of predominant nonequilibrium regions in the shock layer of the model and consequent increase of radiative intensity.

To explain some of the noted characteristics of the experimental spectra discussed above, calculations were made of the model heating transient during flight, taking into account both convective and radiative sources. The results indicate that the aluminum model surface is not melting or ablating (surface temperature less than about 935°K) when the model passes the radiometers. Thus, it is reasoned that this spectrum is representative of air radiation. On the other hand, calculations show the plastic models are ablating and, in fact, tests described in detail in reference 21 have shown that this excessive infrared radiation most probably is emitted by ablation products in the surface boundary layer. Therefore, it is concluded that the spectrum observed in the ultraviolet, from 0.2 to 0.5 micron, for all model materials, except polycarbonate, is due to air since the agreement among the present experiments and theory at high flight densities is excellent. In contrast, the majority of radiation observed in the infrared is considered due to sources other than air.

BROADBAND RADIOMETER RESULTS

Equilibrium Air Radiation

Observations of model shock-layer radiation were made with broadband radiometers for a wide range of velocities and densities. The S-5 spectral response of the phototube cathode material was chosen from the commercially available surfaces in order to observe as much of the anticipated air radiation as was possible. Figure 5 depicted this spectral response and contrasted it with the spectral response of the narrow-band radiometers. The broadband radiometer measurements, which are listed along with the flight conditions and the reduced form of the data in table I, are considered closely representative of the air radiation present for two important reasons demonstrated in the previous section: (a) most of the intense air radiation occurs in the spectral range from 0.2 to 0.5 micron, the response range of the broadband radiometer, and (b) the extraneous radiation present, when ablating plastic models were observed (except polycarbonate), is concentrated in the infrared spectral range, above 0.5 micron. There is, therefore, a good spectral separation of the two sources of radiation. Further, to make the present broadband results more useful and convenient for correlation and comparison with other work and with theoretical predictions, the observations have been reduced to represent a measure of the total radiation from a unit volume of gas directly behind the normal bow shock of the model. This reduction requires two steps; namely, (a) correction for the portion of the total spectral radiation not seen by the broadband radiometer, and (b) division of the radiative intensity in watts by an equivalent volume of air behind a normal shock wave at the test condition. These two reduction steps are discussed in turn below.

The fraction, F , of the total radiation present responded to by the broadband radiometer is given by

$$F = \frac{\int_0^{\infty} R_{\lambda} W_{\lambda} d\lambda}{\int_0^{\infty} W_{\lambda} d\lambda} \quad (7)$$

Values of F were determined with experimental spectra from narrow-band radiometer test results obtained from the flight of aluminum models. The experimental spectra were arbitrarily terminated at 0.2 and at 1.0 micron. For flight conditions where no aluminum model spectra were available, theoretical values of F were utilized, as computed from the equilibrium air radiation predictions of Meyerott, et al. (ref. 4). The predicted values of E_{λ} instead of W_{λ} were used in the computations, and the spectral range of integration extended over all nonzero values of E_{λ} . The values of F , obtained from the experimental spectra and from the theoretical spectra for a flight velocity near 6.4 km/sec and at various densities, are compared below:

ρ_{∞}/ρ_0	$F_{\text{predicted}}$	$F_{\text{experiment}}$
0.19	0.71	0.61
.076	.67	.58
.019	.62	.66
.006	.60	.64

While for one speed only, the above comparison indicates that the computed values are reasonably accurate, even for cases at the lower densities where most of the radiation is emitted by parts of the flow field that are not in thermodynamic and chemical equilibrium. Nonequilibrium radiation will be discussed in detail in the next section.

Calculation of the equivalent volume of uniform air behind a normal shock wave requires determination of the distribution of relative radiative intensity throughout the shock layer. The effective volume can be defined mathematically with the formula

$$V_{\text{eff}} = \frac{1}{E_t} \int_V E \, dV, \text{ cm}^3 \quad (8)$$

where the integral represents the total radiation being emitted from the portion of the shock layer in view of the radiometer, and E_t is the radiative intensity behind a normal shock wave at the specified conditions. Numerical values for the effective volume for shock layers in equilibrium were found by the reduction procedure described in appendix B.

The procedure is essentially identical in basis to the process used for calculating the theoretical values for W_{λ} previously shown on figure 9, where excellent correspondence between experiment and theory was obtained. Further, measurements of the distribution of equilibrium radiation in shock layers, directly as reported in reference 22 and indirectly as reported in reference 23, show that calculations as used herein predict distributions in close agreement with experiment.

The results of the calculations presented in appendix B indicate that the effective volume depends upon the R/d of the model, upon free-stream velocity to some extent, and very little upon free-stream density. A typical variation of the ratio of effective volume to the total volume of the shock layer for $R/d = 0.714$ is from 0.34 to 0.25 as velocity increases from 6.1 to 11.0 km/sec.

In summary, the value of E_t is derived from the data with the equation

$$E_t = \left(\frac{W_{\text{obs}}}{F} \right) \frac{1}{V_{\text{eff}}} \quad (9)$$

The values of E_t , determined from the broadband radiometer tests, performed in both the pilot and prototype facilities, are presented in table I. Figure 10 displays a selected portion of the results, restricted to high flight

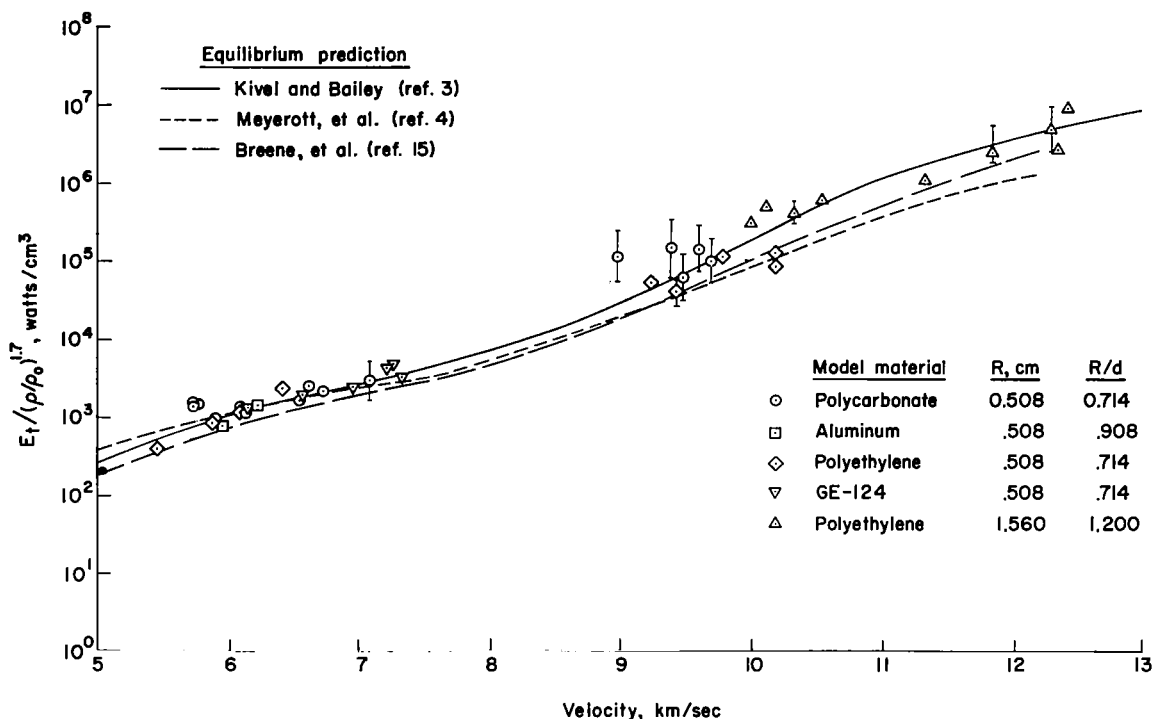


Figure 10.

densities so that only observations of shock layers which are considered predominantly in thermodynamic and chemical equilibrium are included. The density above which results were considered in equilibrium was deduced from the present results as will be shown subsequently and varied from $\rho_{\infty}/\rho_0 = 8 \times 10^{-2}$ at a velocity of 6 km/sec to about $\rho_{\infty}/\rho_0 = 2 \times 10^{-3}$ at 11.0 km/sec. The figure shows the effects on the radiative intensity of several parameters: velocity, density, and the material of which the models were machined. The intensity of radiation is presented with the normalizing factor $(\rho/\rho_0)^{1.7}$, since both the experiments and the equilibrium radiation predictions shown indicate that the intensity should vary approximately to this power of the shock-layer density at a constant velocity. The three predictions are shown for the median shock-layer density at which the data were obtained at any given velocity. This method of presentation allows a convenient and direct comparison between the experimental results and the equilibrium predictions.

The figure brings to attention several interesting points which should be remarked upon. The predictions of Kivel and Bailey, and Meyerott, et al. (refs. 3 and 4) are in excellent agreement with the experimental results in the lower speed range of 5.5 to 7.0 km/sec. This result is not surprising, since the predictions are basically dependent upon shock-tube results which were obtained under essentially similar conditions of gas temperature and density. Such a comparison in fact shows primarily that the present experimental techniques and the shock-tube techniques give closely comparable results. At the higher velocities, approaching and beyond Earth escape speed, it appears that the mean of the experimental results tends to support the higher predictions of

Kivel and Bailey. It must be remarked, however, that the scatter in the experimental results is large, and the lack of extensive data above Earth escape speed makes it difficult to choose among the predictions.

Another feature of the data shown on figure 10 is the lack of any systematic change in the measured equilibrium radiation as a function of the model material. This fact supports the previous conclusion that ablation products radiation falls outside the spectral response region of the broadband radiometer.

In summary, we can see from the figure that the comparisons shown suggest that a reasonably quantitative definition of the intensity of equilibrium radiation has been obtained for conditions corresponding to flight velocities up to 12.4 km/sec. Greater spectral coverage, along with more precise control of experimental conditions are required, however, to improve the accuracy with which we can predict equilibrium radiation intensities at the higher speeds.

Nonequilibrium Air Radiation

When free-stream density is lowered beyond a certain level, excess radiation, above that expected for an equilibrium shock layer, is observed.

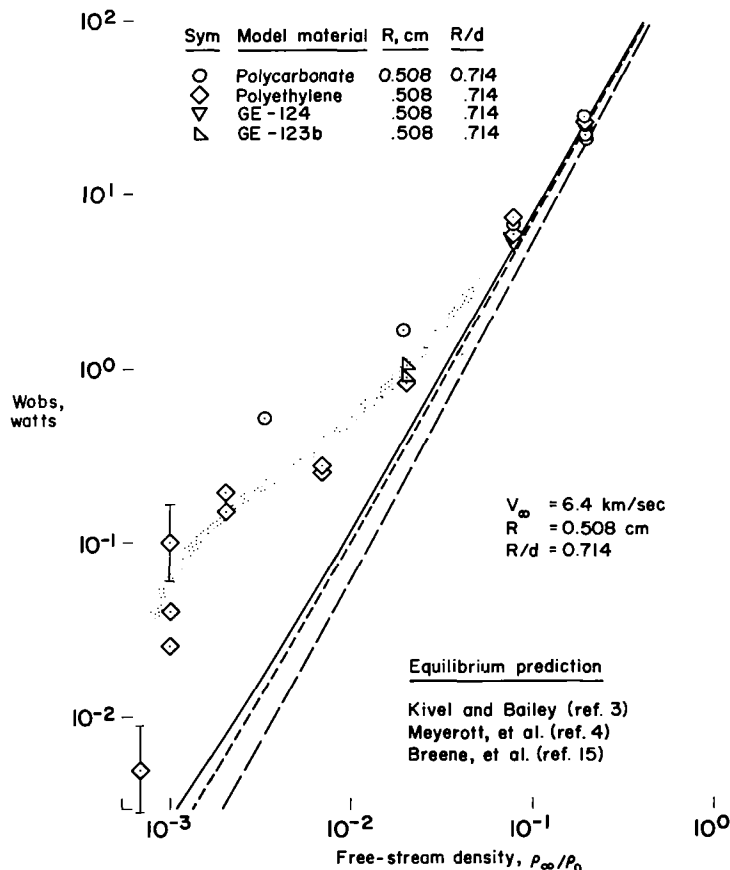


Figure 11.

This is shown by the plot of broadband radiometer results as a function of free-stream density for a velocity of 6.4 km/sec given in figure 11. Experimental values of W_{obs} are compared with equilibrium predictions for W_{obs} computed from references 3, 4, and 15, utilizing values of F and V_{eff} in the formula $W_{obs} = FV_{eff}E_t$ as previously described. The data have been corrected to a common velocity by applying small corrections, proportional to V_{∞}^8 , as deduced from the general trend of the data with velocity. A departure of the measurements from the equilibrium prediction is evident at free-stream densities below about $\rho_{\infty}/\rho_0 = 7 \times 10^{-2}$. Contrary to what might be expected from consideration of the nonequilibrium zone model discussed earlier, the value of W_{obs} does not show the expected approach to a constant value as density is reduced. Instead a continuous decay with decreasing density is observed.

This behavior can be explained in a simple manner by considering the radiation distribution in the shock layer as shown in figure 12. The figure depicts the change in the streamline radiation pattern as a function of streamline position along the shock front and truncation of the radiation by the corner expansion fan. As the density is reduced, the length of the nonequilibrium zones continuously increase until the time required for the flow along streamlines to reach equilibrium conditions becomes greater than the residence time of the gas in the shock layer. Smaller and smaller portions of the nonequilibrium zones exist in the bow shock layer and the total radiation observed should decrease continuously with density instead of taking on a fixed and constant value. It can be further remarked that the radiation from the gas leaving the shock layer through the expansion fan at the model corner is quickly quenched, even at low densities. This is evidenced by radiometric measurements of the flight of nonablating aluminum models showing no increase in radiation when the sides of the model come into view (see, e.g., fig. 6).

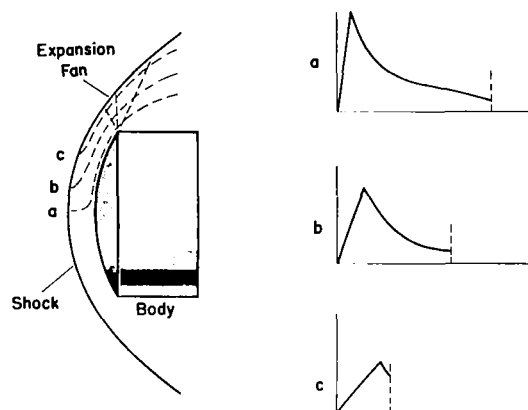


Figure 12.

The variation of the observed radiation as a function of free-stream density at low densities leads to complication in the evaluation of the radiative intensity from the truncated nonequilibrium zone. Now it is desired to (a) evaluate the magnitude of radiation from the nonequilibrium zone, (b) compare the results with those obtained in one-dimensional flow (i.e., shock-tube results), and (c) provide a basis for estimating the magnitude of nonequilibrium radiation for full-scale vehicles, in particular, the flux falling on the body surface. To satisfy these requirements, the experimental observations were reduced to the form

$$I = \frac{1}{2} \int_R^{R+\delta} E(0,r) dr, \text{ watts/cm}^2 \quad (10)$$

where the integration was performed along the stagnation streamline from shock to body. Figure 13 is a sketch of the body shock layer defining the geometric symbols introduced in the equation. The symbol I represents the radiative flux per unit frontal area emitted either upstream or downstream of the shock layer from the gas located along the axis of symmetry. Immediately apparent is the close analogy to the reduction of the equilibrium data where E_t was evaluated, since very nearly

$$I = \left(\frac{E_t}{2} \right) \delta, \text{ watts/cm}^2 \quad (11)$$

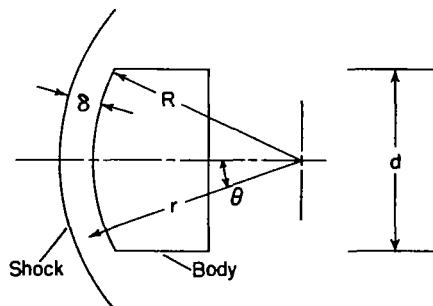


Figure 13.

for equilibrium shock layers. An additional desirable feature is the close relationship to the flux falling on the body surface. For example, Wick in reference 24 gives \dot{q}_R at the stagnation point typically as 84 percent of $(E_t/2)\delta$ for equilibrium shock layers.

What fundamentally is required for the evaluation of I from the experimental data is knowledge of the relative distribution of radiation in the nonequilibrium shock layer. In that which follows we describe the computational technique for determining I from the present experimental observations. Instead of an effective radiating volume which was used to aid in the evaluation of equilibrium values of E_t , we define an effective radiating frontal area with the expression

$$I = \frac{1}{A_{\text{eff}}} \left(\frac{W_t}{2} \right), \text{ watts/cm}^2 \quad (12)$$

where $W_t = W_{\text{obs}}/F$. Again, for equilibrium shock layers

$$I = \frac{1}{A_{\text{eff}}} \left(\frac{W_t}{2} \right) = \left(\frac{E_t}{2} \right) \delta \quad (13)$$

Hence,

$$A_{\text{eff}} = V_{\text{eff}}/\delta \quad (14)$$

For nonequilibrium shock layers, the effective area as defined in equation (12) can be written in integral form as

$$A_{\text{eff}} = \frac{\int_V E(\theta, r) dV}{\int_R^{R+\delta} E(0, r) dr} \quad (15)$$

where $E(\theta, r)$ in the volume integral represents the distribution of radiation in the shock layer.

The integrals of equation (15) were evaluated for one set of flight conditions and for three values of R/d by establishing an approximation to the distribution of radiation under nonequilibrium conditions by the following process: (a) It is assumed that the one-dimensional nonequilibrium zone model can be applied to streamline flow in the shock layer by matching the excitation and relaxation times of the nonequilibrium radiation pattern. Thus, along any streamline the radiation history is given by $E(t)$ from the one-dimensional model and, in particular, along the stagnation streamline from shock to body

$$I = \frac{1}{2} \int_0^t E(t)u(t)dt = \frac{1}{2} \int_R^{R+\delta} E(0,r)dr \quad (16)$$

where $u(t)$ is the velocity distribution. (b) The shock-layer distribution of streamlines and local stream velocity along streamlines were determined from the results of an electronic machine computing program¹ designed to give the thermodynamic and chemical properties in the nonequilibrium shock layer of a hypersonic vehicle. (c) Calculations were then performed along five streamlines crossing the bow shock at equal intervals of θ . For the free-stream density and shock strength at the beginning of each streamline, the location of δ_E and δ_R was established from the excitation and relaxation times measured in one-dimensional flow reported in reference 18. The normal shock laboratory times observed during the referenced experiments were converted to actual residence times by an estimated velocity history faired through the following three points: 1/6 of free-stream velocity (perfect gas theory) directly behind the shock front, 1/9 of free-stream velocity (assumed vibrational equilibrium) at the radiation excitation time, and 1/15 of free-stream velocity (complete thermodynamic equilibrium) at and beyond the radiation relaxation time. (d) Next an approximate nonequilibrium radiation distribution was established along each streamline. This was done by allowing the radiation to start from zero at the shock front, increase linearly with time to a value E_p at the location δ_E , and then to diminish exponentially to a value of $1.1 E_{eq}$ at the location δ_R . Values for E_{eq} , the equilibrium radiation level, beyond the location of δ_R along the streamlines were obtained from an equilibrium solution for the shock layer. Values for E_p were chosen as appropriate for the effective shock strength at the beginning of each streamline. Further, values for E_p were not immediately available, but were obtained by an iterative process. Briefly, the magnitude and velocity dependence for E_p were determined by noting the magnitude and velocity dependence of I as determined from the present tests and adjusting E_p until the computed values for I agreed with observation. It was found that the expression best describing the value of E_p over the velocity range of 6.4 to 11.0 km/sec is

$$E_p = 8.2 \times 10^{-4} \left(\frac{\rho_\infty}{\rho_0} \right) V_\infty^9, \text{ watts/cm}^3 \quad (17)$$

(e) The results of the streamline plotting process were crossplotted to give the radiation distribution as a function of r for fixed values of θ , as

¹Particular results from this "finite rate bow-shock program" were kindly loaned to the authors by Dr. C. E. Treanor of Cornell Aeronautical Laboratories, Inc. The computations were for a hemispherical body of 0.5-cm nose radius flying at $V_\infty = 9.75$ km/sec at $\rho_\infty/\rho_0 = 2.25 \times 10^{-3}$. Reference 20 contains a description of the computing program and results of similar computations.

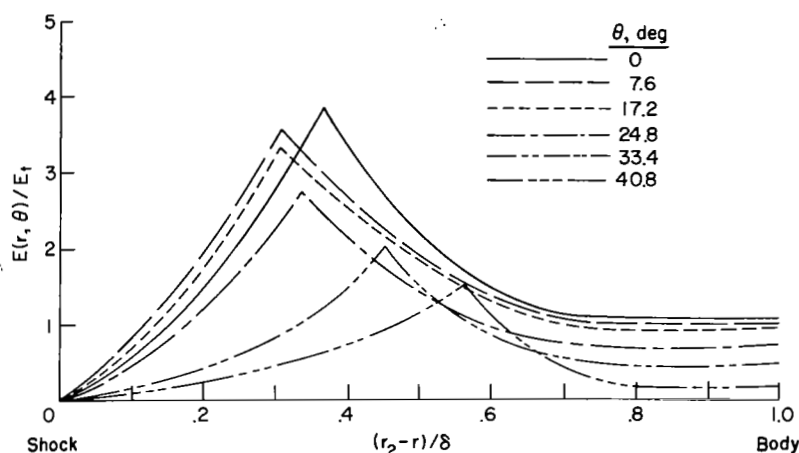


Figure 14.

shown in figure 14 for $R/d = 0.714$. In this example, δ_R is almost uniformly located about $3/4$ of the distance from the shock to the body. These distributions were then used to graphically evaluate the integrals of equation (15). Corrections for that portion of the shock layer hidden from view of the radiometer were accounted for by assuming the same fraction hidden from view as was computed for the equilibrium shock layer case. In

any event, the correction is not large, varying from 19 to 28 percent of the total radiation present, depending upon the R/d of the model.

The resultant values for A_{eff} , after normalization with the spherical surface area of the model face, are shown in the second column below for a free-stream velocity of 9.75 km/sec, a free-stream density of $\rho_\infty/\rho_0 = 2.25 \times 10^{-3}$, and for three values of R/d .

R/d	Nonequilibrium, A_{eff}/A_{total}	Equilibrium, A_{eff}/A_{total}
0.714	0.45	0.27
.908	.61	.40
1.200	.76	.53

Equivalent values of A_{eff}/A_{total} for an equilibrium shock layer are shown in the third column for comparison. As can be seen, the effective areas for the nonequilibrium shock layer are larger, the greatest difference shown here occurring for $R/d = 0.714$ and amounting to an increase of 1.67. Fundamentally, changes in the effective area from nonequilibrium to equilibrium conditions reflect a change in the variation with θ of radiation in the model shock layer. Thus, the nonequilibrium shock layer is predicted to have higher relative levels of radiation away from the stagnation region than for the equilibrium shock layer. The direct cause of these higher levels as will be demonstrated subsequently is the lower velocity dependence of the magnitude of nonequilibrium radiation with respect to the magnitude of equilibrium radiation.

Since the calculations for nonequilibrium effective areas were few in number, values for other velocities were estimated. Below the computed density for which $\delta_R = 3/4\delta$, a fixed nonequilibrium value was assigned. This value was obtained from the ratio of equilibrium to nonequilibrium effective areas in the above table and from the equilibrium effective area computed for the same

density and velocity. For intermediate densities, a smooth variation of effective area from the equilibrium to the nonequilibrium value was assumed.

The results of the evaluation of I from the experimental measurements are presented in figures 15, 16, and 17 as a function of free-stream density at three velocities. Since the data were obtained at various velocities, grouped about the referenced values noted, it was necessary to crossplot the results in order to obtain the presentations shown. Included on the figures are the equilibrium radiation predictions from the previously noted sources (refs. 3, 4, and 15). A band is sketched through the data points to show more clearly their variation with density.

At the higher free-stream densities, the experimental data correspond with the equilibrium radiation predictions as previously shown on figure 11 and as would be expected from the previous equilibrium comparisons made in figure 10. As the density is continually reduced, however, the observed intensities become greater than the equilibrium predictions by an amount which is a direct measure of the excess nonequilibrium radiation behind the shock front. The computed density at which the nonequilibrium zone thickness is three-fourths of the shock standoff distance is marked with an arrow along the line faired through the data points. The most careful calculations of radiation distribution in the shock layer, and thus the best determination of nonequilibrium intensities, were made when

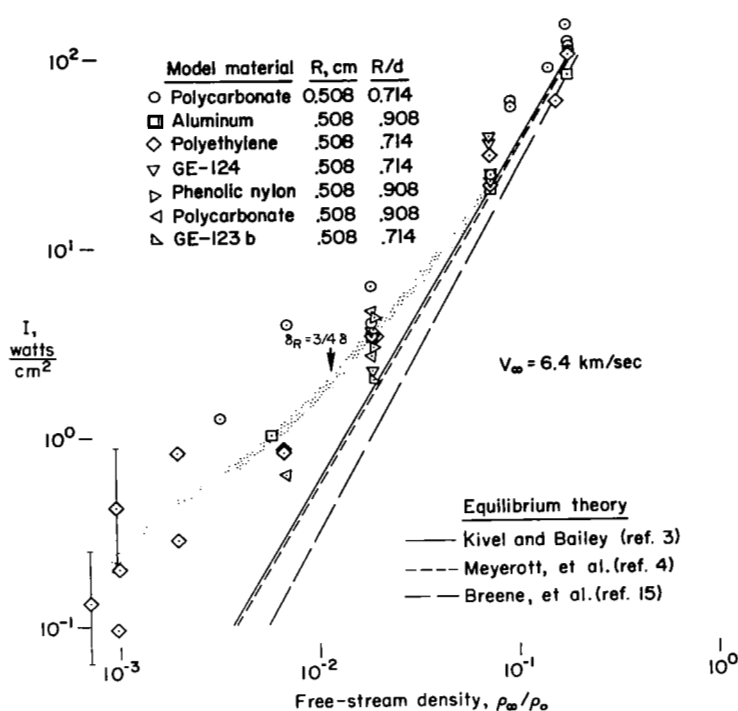


Figure 15.

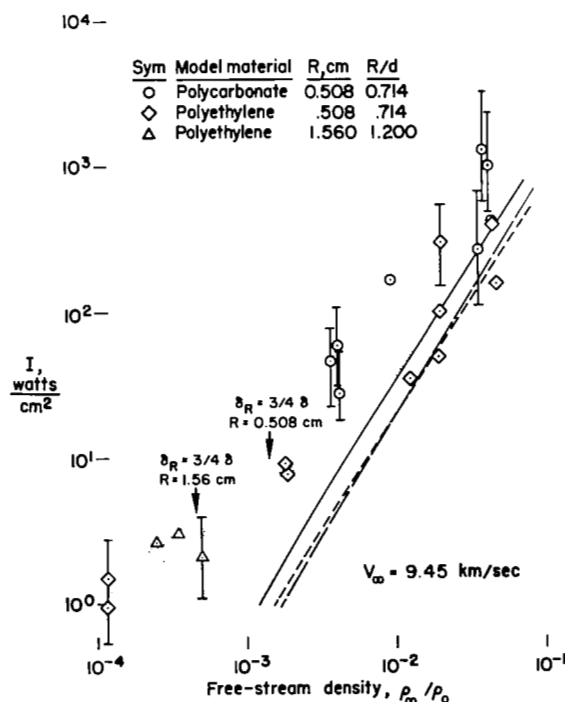


Figure 16.

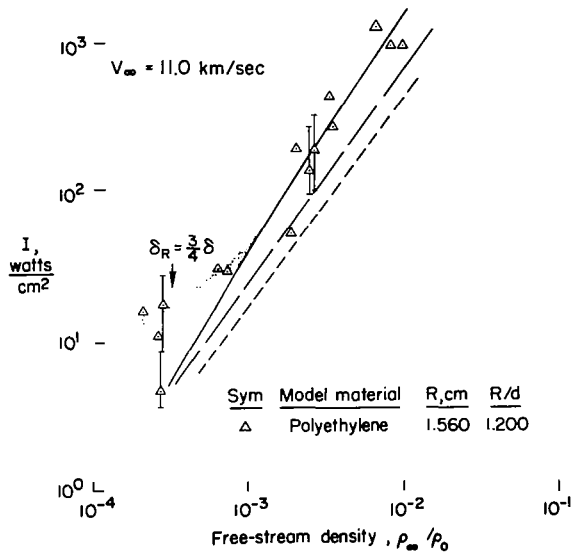


Figure 17.

$\delta_R = 3/4\delta$. The present experiments therefore indicate that the magnitude of the predominantly nonequilibrium radiation along the stagnation streamline for $\delta_R = 3/4\delta$ is 2, 6, and 18 watts/cm² at velocities of 6.4, 9.5, and 11.0 km/sec, respectively. As stream density decreases, the observed radiation intensities continue to decrease as the nonequilibrium zone fills the shock layer and is swept off the body.

COMPARISON OF NONEQUILIBRIUM RADIATION RESULTS WITH SHOCK-TUBE OBSERVATIONS

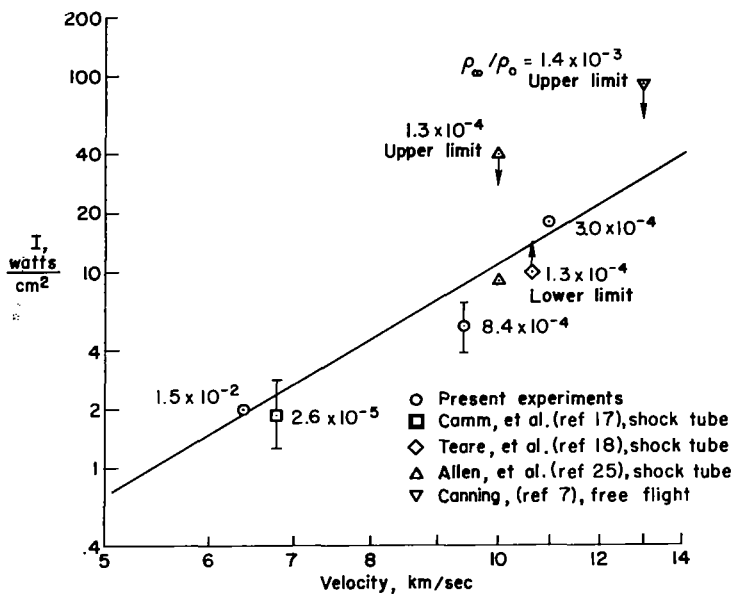


Figure 18.

A summary of measurements of the total intensity of nonequilibrium radiation, which includes available published data obtained from shock tubes (refs. 17, 18, and 25) from earlier free-flight results (ref. 7) and the present results, is given in figure 18. Before proceeding further, it should be reemphasized that the total intensity of nonequilibrium radiation, as measured from the one-dimensional flow pattern behind a normal shock in shock-tube experiments and from the three-dimensional flow pattern along the stagnation streamline in the shock layer of a blunt body, should by no means be expected to agree perfectly. Differences

must occur because of the different velocity history and, consequently, the different distribution of residence time of the radiating particles as the gas flows downstream from the shock front to δ_R . For example, behind a normal shock the gas velocity at δ_R , relative to the shock front, is determined by the equilibrium density ratio across the shock front. A typical value is 1/15 of free-stream velocity for hypersonic speeds. On the other hand, if δ_R is near the body surface in a bow-shock layer, the velocity relative to the shock

front is substantially less than $1/15 V_\infty$ and is approaching zero. Quantitatively, the differences in velocity (see eq. (16)) suggest the bow-shock layer should exhibit lower values for I than those from a one-dimensional normal shock in all cases where δ_R is a substantial fraction of δ .

In figure 18, the earlier free-flight result plotted is not considered well determined but is included in this comparison because of the high velocity at which it was obtained. The intensity shown has been interpreted from the data as representing an upper limit to the nonequilibrium radiation in the spectral range 0.2 to 1.0 micron. The shock-tube measurement reported by Allen, et al., in reference 25 is plotted in two ways. The data point marked upper limit is the authors' statement as to a "reasonable upper limit" for the nonequilibrium radiation. The lower data point is the result of an actual integration of the experimental spectral distribution presented in figure 10 of the reference.

Included with each data point on figure 18 is the free-stream density at which the nonequilibrium radiation was measured.

The figure shows that very similar results have been obtained from the various experiments, apparently within almost a factor of 2. There is no trend apparent in the comparison to suggest that the present results are lower in value than the shock-tube results, as would be reasoned from the argument presented in the paragraph above. (The present results are for $\delta_R = 3/48$.) The close correspondence, however, is still quite gratifying when one considers the differences in the experimental methods and the data-reduction processes required to reduce all the results to this form of presentation. Further, there is no apparent density dependence. The lack of any dependence supports the nonequilibrium zone model which predicts that the total radiation from the zone is independent of free-stream density at a fixed velocity.

A further interesting feature of this figure is that it shows a velocity dependence for nonequilibrium radiation substantially lower than that for equilibrium radiation; namely, the nonequilibrium radiation varies approximately as the fourth power of the velocity, whereas figure 10 indicates that the equilibrium radiation varies from the eighth to the sixteenth power of the velocity. If these trends are continued to even higher velocities, it means that the importance of nonequilibrium radiation heating will diminish compared to that of equilibrium radiative heating.

RADIATIVE HEATING OF FULL-SCALE VEHICLES

The foregoing comparisons, which demonstrate that equilibrium radiation from air appears to be fairly well described, and that nonequilibrium radiation is somewhat smaller than previously predicted (cf. ref. 18), will now be utilized in a brief description of methods to predict radiative heat transfer to a full-scale vehicle entering the Earth's atmosphere.

Let us consider, for purposes of discussion, the prediction of the radiative heat flux falling on the stagnation region of a vehicle with nose

radius 1 meter entering the atmosphere at Earth escape speed. We will construct a chart, similar to that of figure 17, to show how the radiative heating flux is expected to vary with free-stream density at the fixed velocity of 11.0 km/sec. First of all, a prediction for the equilibrium radiative flux falling on the stagnation region is given by

$$I = k(E_t/2)\delta \quad (18)$$

Since figure 10 indicates that the present experimental measurements of equilibrium radiation agree best with the predictions of Kivel and Bailey (ref. 3) at this flight speed, E_t is obtained from this reference, or from figure 7 of the present report. The symbol k is a geometric correction factor due to the curved shape of the shock front. For a spherical nose, Wick has computed a k value near 0.84 (ref. 24). The equilibrium shock-wave standoff distance, δ , for this range of velocities can be well approximated by

$$\delta = \frac{3}{4} R \left(\frac{\rho_\infty}{\rho} \right) \quad (19)$$

which closely corresponds to several theoretical and experimental results. Reference 26 presents a summary of this work. Figure 19 shows the results of using the above formulas, along with reference 27 for the shock density ratio, to predict the equilibrium component of the radiative flux falling on the stagnation region. It should be remarked that this equilibrium prediction at densities of $\rho_\infty/\rho_0 = 10^{-3}$ to 10^{-5} is an extrapolation to a combination of density and temperature where no total intensity measurements of equilibrium radiation have yet been reported, either by shock tube or by the present ballistic techniques.

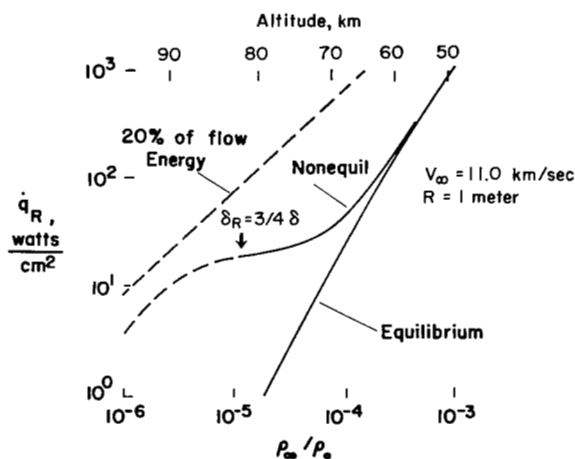


Figure 19.

The nonequilibrium radiative heating contribution for 11.0 km/sec can be estimated directly from figure 18. Since our present best

understanding of the mechanism of nonequilibrium radiation from the zone behind the shock wave is that its magnitude at constant velocity is invariant with density and is not a function of the scale of the vehicle except for the important effects of truncation due to the shock-layer velocity field, we add a constant 18 watts/cm² to the previous equilibrium curve on figure 19 to obtain a prediction of the total radiative flux. We ignore here possible refinements of this nonequilibrium prediction: (a) a "k" correction for the spherical shape of the shock layer, and (b) division of the shock layer into a nonequilibrium part followed by an equilibrium part. Such refinements will change the total prediction by a small amount.

A comment can also be made about the stream density at which the nonequilibrium radiation was measured during the present tests and at what stream density it is of significance for the vehicle size of the present example. As can be seen from figure 17, the nonequilibrium radiation was determined at $\rho_{\infty}/\rho_0 = 3 \times 10^{-4}$ (60 km altitude), whereas figure 19 shows that for the vehicle with a 1 meter nose radius, it is of significance at and below densities of 7×10^{-5} (70 km altitude and up). The extrapolation in density, then, is as little as a factor of 4.

There are further expected effects and interactions which will change the total radiative flux falling on the vehicle stagnation region from the values shown. In order to simplify the discussion of these physical effects they will be described separately, even though in general it can be reasoned that there will be interactions, modifying the total radiation present. All of the effects to be discussed, namely, truncation, flow energy limiting, collision limiting, self-absorption, and merging of boundary layer and shock layer, reduce the radiative heating flux. Truncation by the body velocity field has definitely been observed during the flight of the small models of the present investigation, and its effects have been discussed in the previous section. There is no direct evidence in the present data of the influence of any of the other effects named above. It is felt, however, that a brief description of the expected changes in the radiative heating due to these effects would be instructive.

The density at which truncation is expected to be significant for the example vehicle under discussion is shown on figure 19 by the arrow marked $\delta_R = 3/4\delta$. This density can be obtained by consideration of the laboratory radiative relaxation times reported in reference 18, together with flow-field velocities behind the normal shock and along the stagnation streamline in the shock layer of the vehicle. In the present case, a similar result was obtained by noting that the example vehicle is approximately 60 times larger than the model used to obtain the 11.0 km/sec results shown on figure 17. Since the nonequilibrium zone model indicates that the density for truncation effects would be inversely proportional to vehicle size, truncation for the larger vehicle is expected at a density 60 times lower than that previously computed and shown for the model. In other words, truncation depends upon the ratio δ_R/δ , which is approximately unchanged for constant values of $\rho_{\infty}R$. The expected reduction of the nonequilibrium radiative flux due to increasing amounts of truncation for the example vehicle is shown as the dashed extension to the nonequilibrium curve sketched on the figure.

An important radiation-limiting phenomenon that occurs, but apparently would not influence greatly this particular case to any degree, is flow energy limiting. The total flux of energy per unit time per unit frontal area contained in the flow entering the shock layer of the vehicle is given closely by

$$I = (1/2)\rho_{\infty}V_{\infty}^3, \text{ watts/cm}^2 \quad (20)$$

The radiative flux per unit frontal area of shock layer, in both directions, cannot approach this value too closely because the energy drain would cause the

gas temperature and, consequently, the radiation level to decay grossly as the gas flowed back from the shock front. A reasonable upper limit of 20 percent of the flow energy is plotted on figure 19. Approximately this same upper limit is shown by machine-programmed computer calculations given in figure 14 of reference 28. Either truncation or flow energy limiting would prevent the nonequilibrium radiative flux from exceeding approximately 10 watts/cm² below $\rho_{\infty}/\rho_0 = 10^{-6}$. At the highest densities, approaching sea level, the equilibrium radiative flux would also be limited by the available flux of flow energy.

Collision limiting, discussed in reference 18, is defined in the reference as a reduction of the radiative intensity due to an insufficient number of collisions to maintain the population of excited particles against the drainage by radiation. It would first be expected to reduce the peak value of the nonequilibrium radiation profile. Very little is known about how low the density must become before collision limiting reduces the radiative intensity. The experiments by Allen, et al. (ref. 25) suggest that, at least for one band system, collision limiting may reduce the nonequilibrium radiation significantly at a pressure of 20 microns of Mercury. This represents a density of $\rho_{\infty}/\rho_0 = 2.6 \times 10^{-5}$.

At very high altitudes, merging of the viscous boundary layer and the shock layer occurs and will have a suppressing effect on the small radiative heating levels expected to exist at these altitudes. For example, although it was concluded that it did not significantly influence determination of the nonequilibrium radiative intensity, the boundary-layer thickness in the stagnation region for the present models flown at the higher velocities and at the lowest densities was estimated to be about one-fourth the shock standoff distance. Similarly to the variation of the nonequilibrium-zone thickness and the effects of truncation, the ratio of the boundary-layer thickness to the shock-standoff distance is approximately constant for constant values of $\rho_{\infty}R$. Thus, about the same portion of the shock layer is boundary layer for the 1 meter nose radius vehicle as for the model at a density 60 times lower.

At the lower altitudes, particularly at densities higher than those shown on figure 19, self-absorption of the radiation can suppress the radiative heating; references 28 and 29 give predictions of this phenomenon. The prediction shown in figure 19, then, is considered a radiative heating estimate based on the present state of knowledge. Other than the uncertainty due to the less-than-complete spectral coverage, however, all the effects remarked upon above would lower the radiative heating and not increase it.

CONCLUDING REMARKS

In summary, the results of the present experimental investigation indicate that a fair definition of the radiative properties of air in thermodynamic and chemical equilibrium has been obtained for conditions corresponding to flight velocities of 5.5 to 12.4 km/sec. Predicted equilibrium spectra for the shock layer over the velocity range of 6 to 10 km/sec were in satisfying agreement with observations at high densities where equilibrium conditions are expected. Greater spectral coverage, along with more precise control of experimental

conditions, is required, however, to obtain more definitive results at the higher velocities. The radiation attributed to nonequilibrium effects behind the shock front appears to be reasonably described by the simple binary-collision model of the nonequilibrium zone suitably modified by the effects of truncation. The measured intensity of nonequilibrium radiation has turned out to be rather small, at least up to Earth escape speed and will probably be of little importance, in contrast to the equilibrium radiation, as the velocity is increased even further.

It is believed that the present results demonstrate that additional work in the laboratory should emphasize (a) increased accuracy of measurement, and (b) the study of equilibrium radiative heat transfer at higher speeds, for example, 12 to 18 km/sec, which are of interest for Earth entry for efficient return from the nearby planets. At these velocities, radiative heat transfer is expected to be the dominant heating mechanism; it will probably be the primary factor controlling the vehicle's heat-shield shape. Another problem area still requiring investigation is the scaling or application of what we learn in the laboratory to the full-scale vehicle. Although it is believed we have a fair understanding of how to do this, there is as yet no extensive experimental proof available. Further, as exemplified by the computations of Howe and Viegas (ref. 28), additional studies might be required of the coupling among the convective, radiative, and ablative processes.

Ames Research Center
National Aeronautics and Space Administration
Moffett Field, Calif., Nov. 27, 1963

APPENDIX A

THEORETICAL COMPUTATION OF TOTAL SPECTRAL RADIATION FROM SHOCK LAYER

The total emission from a volume element of the shock layer per unit wavelength is

$$\frac{dW_\lambda}{dV} = E_\lambda, \text{ watts/cm}^3 \text{ micron} \quad (\text{A1})$$

Integrating over the volume observed by the radiometer gives

$$W_\lambda = \int_V E_\lambda dV, \text{ watts/micron} \quad (\text{A2})$$

Constructing a prediction for the spectrum W_λ from the above formula requires assigning a value of E_λ to each point in the shock layer and performing the indicated integration for every value of wavelength desired. We may also write

$$W_\lambda = E_{t\lambda} V_{\text{eff}}(\lambda) = \int_V E_\lambda dV \quad (\text{A3})$$

where $V_{\text{eff}}(\lambda)$ is an equivalent shock-layer volume satisfying the expression and is a function of λ . The rather extensive calculations outlined above for predicting W_λ were reduced to the evaluation of a single integral by allowing V_{eff} to take on a single value with the approximation

$$V_{\text{eff}} = \frac{\int_V E_\lambda dV}{E_{t\lambda}} \approx \frac{\int_V E dV}{E_t} \quad (\text{A4})$$

where $E = \int_0^\infty E_\lambda d\lambda$ and $E_t = \int_0^\infty E_{t\lambda} d\lambda$. This approximation is equivalent to assuming that the relative spectral distribution of the gas directly behind the normal part of the bow shock layer is representative of the average spectral distribution of all the radiation from the volume in view of the radiometer.

Thus, finally, values for W_λ were computed by use of

$$W_\lambda = E_{t\lambda} V_{\text{eff}} \quad (\text{A5})$$

where $E_{t\lambda}$ is the spectral distribution for conditions directly behind the bow

shock and was obtained (a) by interpolation in the tables of reference 4 and (b) by computation using the scheme outlined in reference 30 but with the transition probabilities given by Kivel and Bailey in reference 3.¹ The required values of effective volume, V_{eff} , were computed as outlined in appendix B.

¹These calculations were made by Victor Reis of Ames Research Center.

APPENDIX B

DETERMINATION OF EFFECTIVE VOLUME FOR EQUILIBRIUM SHOCK LAYER

A measure of the radiative intensity directly behind the normal part of the model bow shock can be obtained from observations of the total shock-layer radiation by defining

$$E_t = \frac{1}{V_{\text{eff}}} \int_V E \, dV \quad (\text{B1})$$

where the integral represents the total radiation viewed by the radiometer from the shock layer and V_{eff} is the effective volume radiating at the specified conditions. The coordinate system in figure 13 is used for the following calculations. Numerical values for V_{eff} were found by solving the above equation using an approximation to the equilibrium radiation distribution throughout the shock layer. The radiation distribution, E , as a function of θ , the angular distance from the stagnation point was obtained in the following manner: (a) The equilibrium temperature and density behind the bow shock were determined by means of charts of equilibrium real-gas properties of air behind normal shock waves (ref. 27) and oblique shock relations. (b) By use of the pressure distributions and the sonic-point locations from reference 31, the equilibrium temperature and density were computed along the constant entropy stagnation streamline which flows along the body surface to the corner of the model face. These pressure distributions are similar to that given by Newtonian theory as long as the sonic point lies on the spherical face. (c) From the temperature and density distributions, the relative equilibrium radiation distribution, E/E_t , as a function of θ was determined from the equilibrium predictions of Kivel and Bailey (ref. 3). The radiation distributions along the shock front and the body surface were then averaged to establish a distribution independent of r , the coordinate normal to the body surface. Figure 20 shows a typical result of this process.

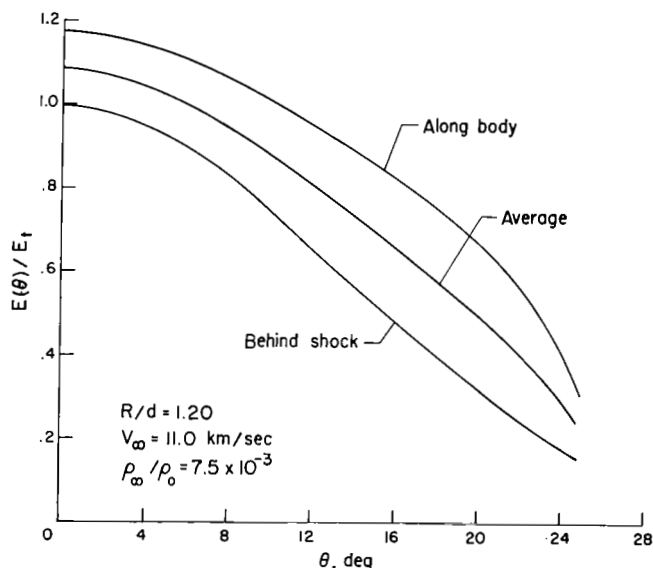


Figure 20.

When a radiometer views the model shock layer at right angles to the flight path, part of the shock layer is hidden by the bulge of the model face. This reduced volume is accounted for by noting that the part of the shock layer visible on the side opposite the radiometer is that between the shock front (assumed herein to be given in spherical polar coordinates as $r_2 = R + \delta = \text{constant}$, where R is the nose radius, and δ is the shock standoff distance) and the cylindrical surface tangent to the model surface and parallel to the radiometer line of sight. The equation of this

surface is given by

$$r_1 = \frac{R}{\sqrt{\sin^2 \theta \cos^2 \varphi + \cos^2 \varphi}} \quad (B2)$$

The expression for the effective volume can now be written as

$$V_{\text{eff}} = \int_0^{\theta_m} \int_R^{r_2} \int_0^\pi r^2 [E(\theta)/E_t] \sin \theta \, d\varphi \, dr \, d\theta \\ + \int_0^{\theta_m} \int_{r_1}^{r_2} \int_0^\varphi r^2 [E(\theta)/E_t] \sin \theta \, d\varphi \, dr \, d\theta \quad (B3)$$

where θ_m is the colatitude of the model, and φ the limit of the integral defined as

$$\varphi_m = \text{const} = \sin^{-1} \left\{ \frac{\sqrt{1 - [R/(R + \delta)]^2}}{\sin \theta_m} \right\} \quad (B4)$$

or

$$\varphi = \sin^{-1} \left\{ \frac{\sqrt{1 - [R/(R + \delta)]^2}}{\sin \theta} \right\} \quad (B5)$$

as dictated by the intersection of the spherical and cylindrical surfaces bounding that part of the shock layer on the side opposite the radiometer. The first integral is straightforward and was evaluated analytically, except for the θ term which required numerical methods. The second integral is of elliptic form and was evaluated similarly to the first integral.

The results of these calculations, normalized by the total shock-layer volume out to the edge of the model face, defined as

$$V_{\text{total}} = \frac{2\pi}{3} R^3 \left[\left(1 + \frac{\delta}{R}\right)^3 - 1 \right] \left\{ 1 - \left[1 - \frac{1}{4(R/d)^2} \right]^{1/2} \right\} \quad (B6)$$

are given in the following table.¹ The values of the ratio of effective volume to total volume show a strong dependence upon R/d , some dependence upon velocity, and to the extent of the available calculations, relatively small dependence upon density. For the data reduction, the value of the effective

¹Calculations of possible additional radiative contributions in view of the radiometer, at the body corner in an equilibrium expansion fan, indicated negligible changes in V_{eff} .

R/d	ρ_{∞}/ρ_0	V_{∞} , km/sec	V_{eff}/V_{total}
0.714	10^{-1}	6.1	0.34
	7.5×10^{-3}	6.1	.34
	2.25×10^{-3}	9.75	.26
	7.5×10^{-3}	11.0	.25
0.908	10^{-1}	6.1	.50
	7.5×10^{-3}	6.1	.49
	2.25×10^{-3}	9.75	.40
	7.5×10^{-3}	11.0	.40
1.200	7.5×10^{-3}	6.1	.57
	2.25×10^{-3}	9.75	.53
	7.5×10^{-3}	11.0	.53

volume was allowed to change smoothly for conditions intermediate between the calculated conditions. The actual values used are listed in table I, page 40.

REFERENCES

1. Meyerott, R. E.: Absorption Coefficients of Air From 6000° K to 18,000° K. USAF Proj. Rand RM1554, The Rand Corp.
2. Kivel, R., Mayer, H., and Bethe, H.: Annals of Physics, vol. 2, 1957.
3. Kivel, B., and Bailey, K.: Tables of Radiation From High Temperature Air. Avco Res. Rep. 21, 1957.
4. Meyerott, R. E., Sokoloff, J., and Nicholls, R. W.: Absorption Coefficients of Air. Geophys. Res. Paper 68, July 1960. (Also LMSD 288052, Lockheed Aircraft Corp., 1959.)
5. Armstrong, B. H.: Absorption Coefficients of Air From 22,000 to 220,000° K. Lockheed Missile Systems Div. Rep. 5135.
6. Page, William A., Canning, Thomas N., Craig, Roger A., and Stephenson, Jack D.: Measurements of Thermal Radiation of Air From the Stagnation Region of Blunt Bodies Traveling at Velocities up to 31,000 Feet per Second. NASA TM X-508, 1961.
7. Canning, Thomas N., and Page, William A.: Measurements of Radiation From the Flow Fields of Bodies Flying at Speeds up to 13.4 Kilometers per Second. Paper presented to the Fluid Mechanics Panel of AGARD, Brussels, Belgium, April 1962.
8. Page, William A.: Shock-Layer Radiation of Blunt Bodies Traveling at Lunar Return Entry Velocities. IAS 63-41.
9. Curtis, John S.: An Accelerated Reservoir Light-Gas Gun. NASA TN D-1144, 1962.
10. Wilkins, Max E., and Carros, Robert J.: Combustion Tests of Oxygen-Hydrogen-Helium Mixtures at Loading Pressures up to 8000 Pounds per Square Inch. NASA TN D-1892, 1963.
11. Seiff, Alvin: A Progress Report on the Ames Hypervelocity Free-Flight Facilities and Some Current Research Problems Being Studied in Them. AIAA 63-162.
12. Stair, Ralph, Johnston, Russell G., and Halbach, E. W.: Standard of Spectral Radiance for the Region of 0.25 to 2.6 Microns. Jour. of Res. of the Nat. Bur. of Stds. A. Phys. and Chem., vol. 64A, no. 4, July-August 1960.
13. Nicholls, R. W.: Studies Upon Transition Probabilities and Molecular Excitation. Annales de Geophysique, vol. 14, 1958, pp. 208-224.

14. Keck, J. C., Allen, R. A., and Taylor, R. L.: Electronic Transition Moments for Air Molecules. Avco-Everett Res. Rep. 149, March 1963.
15. Breene, R. G., Nardone, Maria, Riethof, T. R., and Zeldin Saydean: Radiance of Species in High Temperature Air. GE R62SD52, G. E. Space Sci. Lab., July 1962.
16. Kivel, Bennett: Radiation From Hot Air and Stagnation Heating. Avco-Everett Res. Rep. 79, 1959.
17. Camm, J. C., Kivel, B., Taylor, R. L., and Teare, J. D.: Absolute Intensity of Nonequilibrium Radiation in Air and Stagnation Heating at High Altitudes. Avco-Everett Res. Rep. 93, 1959.
18. Teare, J. D., Georgiev, S., and Allen, R. A.: Radiation From the Nonequilibrium Shock Front. Avco-Everett Res. Rep. 112, 1961.
19. Kivel, B., Hammerling, P., and Teare, J. D.: Radiation From the Nonequilibrium Region of Normal Shocks in Oxygen, Nitrogen and Air. Phys. Chem. in Aerodynamics and Space Flight, pp. 132-137.
20. Hall, J. Gordon, Eschenroeder, Alan Q., and Marrone, Paul V.: Inviscid Hypersonic Airflows With Coupled Nonequilibrium Processes. Cornell Aero. Lab. Rep. AF-1413-A-2, May 1962.
21. Craig, Roger A., and Davy, William C.: Thermal Radiation From Ablation Products Injected Into a Hypersonic Shock Layer. NASA TN D-1978, 1963.
22. Givens, John, Canning, Thomas N., and Bailey, Harry: Measurements of Spatial Distribution of Shock Layer Radiation for Blunt Bodies at Hypersonic Speeds. NASA TM X-852, 1963.
23. Walters, Edward E.: Free-Flight Measurements of Radiative Heating to the Front Face of Apollo Reentry Capsule as a Function of Angle of Attack. NASA TM X-851, 1964.
24. Wick, Bradford H.: Radiative Heating of Vehicles Entering the Earth's Atmosphere. Paper presented to the Fluid Mechanics Panel of AGARD, Brussels, Belgium, April 1962.
25. Allen, R. A., Rose, P. H., and Camm, J. C.: Nonequilibrium and Equilibrium Radiation at Super-Satellite Re-Entry Velocities. IAS 63-77.
26. Seiff, Alvin: Recent Information on Hypersonic Flow Fields. Proc. NASA - Univ. Conf. on Sci. and Tech. of Space Exploration, Chicago, Illinois. NASA SP-24, Sept. 1962.
27. Ziemer, R. W.: Extended Hypervelocity Gas Dynamic Charts for Equilibrium Air. Space Tech. Lab. TR-60-0000-09093, 1960.

28. Howe, J. T., and Viegas, J. R.: Solutions of the Ionized Radiating Shock Layer, Including Reabsorption and Foreign Species Effects, and Stagnation Region Heat Transfer. NASA TR R-159, 1963.
29. Yoshikawa, Kenneth K., and Chapman, Dean R.: Radiative Heat Transfer and Absorption Behind a Hypersonic Normal Shock Wave. NASA TN D-1424, 1962.
30. Keck, James C., Camm, John C., Kivel, Bennett, and Wentink, Tunis, Jr.: Radiation From Hot Air, Part II. Shock Tube Study of Absolute Intensities. Annals of Physics, vol. 7, no. 1, May 1959.
31. Kaattari, George E.: Predicted Gas Properties in the Shock Layer Ahead of Capsule-Type Vehicles at Angles of Attack. NASA TN D-1423, 1962.

TABLE I.- SUMMARY OF EXPERIMENTAL DATA

V_{∞} , km/sec	ρ_{∞}/ρ_0	ρ/ρ_0	T, °K	W_{obs} , watts	V_{eff} , cm ³	F	E_t , watts/cm ³	Model material ¹
Prototype facility data; R/d = 1.20, R = 1.56 cm								
12.41	0.00198	0.0300	13,600	338	0.0600	0.25	22,500	PE ²
12.35	.00185	.0277	13,700	87.6	.0607	.25	5,770	PE ²
12.30	.00257	.0388	13,500	282	.0604	.25	18,700	PE ^{2,3}
11.85	.00246	.0365	13,000	176	.0615	.33	8,670	PE ²
11.55	.000209	.00340	11,100	27.4	.0558	.54	909	PE ²
11.53	.000280	.00452	11,200	28.5	.0563	.52	973	PE ^{2,3}
11.50	.000271	.00440	11,200	7.68	.0281	.52	526	PE ^{2,4}
11.39	.000262	.00420	11,300	15.7	.0569	.53	520	PE ^{2,4}
11.33	.00939	.130	13,200	832	.0660	.38	33,200	PE ²
11.25	.000626	.00980	11,400	40.0	.0581	.52	1,320	PE ²
11.18	.000721	.0111	11,600	34.9	.0592	.51	1,150	PE ²
10.52	.00801	.112	11,800	409	.0647	.49	14,800	PE ²
10.32	.00341	.0506	10,800	95.8	.0615	.60	2,590	PE ^{2,4}
10.10	.00316	.0471	10,600	108	.0614	.63	2,790	PE ²
9.98	.00642	.0937	10,500	223	.0617	.65	5,560	PE ²
9.72	.000352	.00570	9,230	5.72	.0562	.78	131	PE ²
9.50	.000503	.00810	9,020	3.70	.0566	.82	79.8	PE ^{2,4}
9.23	.000250	.00418	8,360	4.19	.0543	.83	93.0	PE
Pilot facility data; R/d = 0.714, R = 0.51 cm								
10.18	.0195	.267	11,700	19.8	.00341	.43	13,500	PE ²
10.17	.0478	.650	12,100	62.3	.00343	.44	41,300	PE ²
9.81	.00370	.0548	11,200	12.8	.00322	.47	8,470	PC ²
9.77	.0454	.626	11,300	85.6	.00349	.47	51,900	PE ²
9.72	.00414	.0617	10,100	4.56	.00162	.49	8,600	PC ^{2,4}
9.68	.0453	.625	11,000	80.9	.00351	.50	46,100	PC ²
9.60	.0384	.530	10,900	42.2	.00177	.48	49,400	PC ^{2,4}
9.46	.0365	.540	10,800	35.0	.00356	.51	19,300	PC ^{2,4}
9.41	.0128	.181	10,200	3.80	.00349	.50	2,180	PE ²
9.37	.0424	.589	10,500	108	.00356	.49	62,000	PC ^{2,5}
9.31	.00424	.0604	9,500	4.70	.00327	.51	2,820	PC ^{2,4}
9.22	.00942	.135	9,780	20.7	.00347	.52	11,500	PC ²
9.22	.0194	.273	9,970	10.7	.00352	.52	5,850	PE ²
9.14	.000126	.00217	8,000	.0631	.00399	.52	30.4	PE ^{4,7}
9.14	.000126	.00217	8,000	.0998	.00399	.52	48.1	PE ⁷
8.97	.0397	.552	9,900	84.6	.00368	.55	48,800	PC ^{2,4}
8.78	.00182	.0287	8,470	1.68	.00324	.54	961	PE
8.61	.00187	.0296	8,340	1.30	.00328	.55	720	PE
8.14	.00680	.103	8,140	1.62	.00356	.58	784	PC ⁴

¹PE, polyethylene; PC, polycarbonate; AL, aluminum; 24, G.E. 124; 23, G.E. 123b; PN, phenolic nylon.

²Shot made into advancing airstream.

³No airstream data, calibration data used.

⁴High angle of attack.

⁵Radiation trace offscale, estimated value.

⁶R/d = 0.908.

⁷From reference 7.

TABLE I.- SUMMARY OF EXPERIMENTAL DATA - Concluded

V_{∞} , km/sec	ρ_{∞}/ρ_0	ρ/ρ_0	T, °K	W _{obs} , watts	V _{eff} , cm ³	F	E _t , watts/cm ³	Model material
7.31	0.0195	0.271	7,900	0.924	0.00408	0.62	364	24
7.25	.0767	1.03	8,220	14.8	.00428	.66	5,240	24
7.22	.000720	.0117	6,570	.013	.00352	.52	7.09	PE ⁴
7.20	.0767	1.03	8,200	13.2	.00429	.67	4,590	24
7.07	.152	1.98	8,600	28.6	.00449	.66	9,660	PC ⁴
6.99	.0195	.265	7,700	1.36	.00429	.62	511	23
6.98	.00720	.105	7,400	1.38	.00398	.60	578	PC
6.94	.0194	.263	7,680	1.24	.00430	.63	456	PE
6.94	.0761	.997	8,090	7.14	.00447	.67	2,380	24
6.82	.0190	.256	7,600	1.26	.00445	.63	448	24
6.81	.0197	.264	7,650	1.26	.00378	.63	529	PC ⁶
6.74	.0070	.0987	7,020	.162	.00364	.61	73.0	PC ⁶
6.71	.190	2.38	8,280	31.8	.00475	.71	94.3	PC
6.71	.00100	.0153	6,500	.0605	.00386	.55	28.4	PE
6.71	.0195	.259	7,540	1.14	.00386	.63	467	PN ⁶
6.67	.0200	.265	7,510	1.14	.00450	.63	402	PE
6.61	.0020	.0291	6,720	.257	.00408	.58	108	PE
6.61	.0195	.257	7,460	1.360	.00454	.63	477	23
6.60	.188	2.33	8,200	35.7	.00485	.69	10,700	PC
6.56	.0192	.251	7,380	2.04	.00458	.63	707	PC
6.55	.0770	.980	7,760	6.12	.00469	.68	1,920	24
6.53	.192	2.36	8,140	24.6	.00492	.70	7,150	PC
6.49	.000980	.0146	6,400	.114	.00403	.51	55.4	PE ⁵
6.47	.0191	.246	7,760	.824	.00405	.62	328	AL ⁶
6.41	.00690	.0938	6,880	.264	.00445	.62	95.8	PE
6.40	.0767	.966	7,650	7.30	.00482	.69	2,200	PE
6.36	.000982	.0143	6,300	.0244	.00414	.51	11.5	PE
6.40	.00594	.0790	6,830	.0780	.00130	.60	99.6	AL ^{4,6}
6.31	.00691	.0926	7,510	.246	.00455	.60	90.3	PE
6.22	.0750	.922	7,460	3.51	.00425	.67	1,230	AL ⁶
6.13	.0767	.940	7,400	4.13	.00508	.69	1,180	24
6.12	.191	2.30	7,920	17.4	.00520	.71	4,720	PC ⁴
6.08	.0195	.243	7,050	.584	.00501	.64	182	23
6.08	.0768	.937	7,430	3.90	.00513	.70	1,080	PE
6.07	.0774	.944	7,430	4.50	.00511	.70	1,260	PC
6.04	.00329	.0438	6,500	.336	.00465	.58	124	PC
5.96	.0189	.230	6,880	1.19	.00514	.65	357	PC
5.94	.190	2.20	7,650	9.60	.00465	.71	2,920	AL ⁶
5.94	.0197	.233	6,940	.60	.00441	.65	209	PC
5.94	.0192	.234	6,880	1.26	.00514	.65	378	PC
5.88	.190	2.18	7,570	14.85	.00551	.72	3,740	PC
5.86	.192	2.21	7,680	12.9	.00546	.72	3,280	PE
5.77	.0020	.0252	6,170	.0667	.00499	.55	24.3	PE
5.74	.0978	1.12	7,180	7.24	.00550	.71	1,850	PC
5.72	.0760	.882	7,020	42.6	.00548	.70	1,110	PC
5.72	.0978	1.12	7,160	7.24	.00552	.71	1,850	PC
5.68	.0192	.225	6,660	.452	.00542	.65	128	PC
5.61	.0189	.219	6,590	.851	.00553	.66	232	PC
5.58	.0197	.228	6,530	.600	.00474	.65	195	PN ⁶
5.44	.167	1.77	7,130	4.80	.00614	.73	1,070	PE
5.40	.0191	.216	6,390	.452	.00575	.66	119	PC

"The National Aeronautics and Space Administration . . . shall . . . provide for the widest practical appropriate dissemination of information concerning its activities and the results thereof . . . objectives being the expansion of human knowledge of phenomena in the atmosphere and space."

—NATIONAL AERONAUTICS AND SPACE ACT OF 1958

NASA SCIENTIFIC AND TECHNICAL PUBLICATIONS

TECHNICAL REPORTS: Scientific and technical information considered important, complete, and a lasting contribution to existing knowledge.

TECHNICAL NOTES: Information less broad in scope but nevertheless of importance as a contribution to existing knowledge.

TECHNICAL MEMORANDUMS: Information receiving limited distribution because of preliminary data, security classification, or other reasons.

CONTRACTOR REPORTS: Technical information generated in connection with a NASA contract or grant and released under NASA auspices.

TECHNICAL TRANSLATIONS: Information published in a foreign language considered to merit NASA distribution in English.

TECHNICAL REPRINTS: Information derived from NASA activities and initially published in the form of journal articles or meeting papers.

SPECIAL PUBLICATIONS: Information derived from or of value to NASA activities but not necessarily reporting the results of individual NASA-programmed scientific efforts. Publications include conference proceedings, monographs, data compilations, handbooks, sourcebooks, and special bibliographies.

Details on the availability of these publications may be obtained from:

SCIENTIFIC AND TECHNICAL INFORMATION DIVISION
NATIONAL AERONAUTICS AND SPACE ADMINISTRATION

Washington, D.C. 20546